

# Interface engineering of van der Waals heterostructures towards energy-efficient quantum devices operating at high temperatures

Manh-Ha Doan<sup>1\*</sup> and Peter Bøggild<sup>1\*</sup>

<sup>1</sup> Department of Physics, Technical University of Denmark, Kgs. Lyngby 2800, Denmark

\*E-mail: [mando@dtu.dk](mailto:mando@dtu.dk) and [pbog@dtu.dk](mailto:pbog@dtu.dk)

## Abstract

Quantum devices, which rely on quantum mechanical effects for their operation, may offer advantages, such as reduced dimensions, increased speed, and energy efficiency, compared to conventional devices. However, quantum phenomena are typically observed only at cryogenic temperatures, which limits their practical applications. Two-dimensional materials and their van der Waals (vdW) heterostructures provide a promising platform for high-temperature quantum devices owing to their strong Coulomb interactions and/or spin-orbit coupling. In this review, we summarise recent research on emergent quantum phenomena in vdW heterostructures based on interlayer tunnelling and the coupling of charged particles and spins, including negative differential resistance, Josephson tunnelling, exciton condensation, and topological superconductivity. These are the underlying mechanisms of energy-efficient devices, including tunnel field-effect transistors, topological/superconducting transistors, and quantum computers. The natural homojunction within vdW layered materials offers clean interfaces and perfectly aligned structures for enhanced interlayer coupling. Twisted bilayers with small angles may also give rise to novel quantum effects. In addition, we highlight several proposed structures for achieving high-temperature Majorana zero modes, which are critical elements of topological quantum computing. This review is helpful for researchers working on interface engineering of vdW heterostructures towards energy-efficient quantum devices operating above liquid nitrogen temperature.

Keywords: *2D materials, tunneling, quantum interference, exciton condensation, superconductivity, topological superconductivity*

## 1. Introduction

Energy consumption is a crucial issue in modern electronics, specifically with high demands for applications in emerging fields, such as artificial intelligence, high-performance computing, and internet communication [1-4]. Field-effect transistors (FET), the fundamental building blocks of computer chips, have been scaled down exponentially in recent decades, a trend known as Moore's law [5, 6]. This scaling, together with the innovation of radical device designs and integration techniques, for example Fin-FET, gate-all-around FET, and monolithic 3D integration, has boosted computing speed while maintaining constant power consumption [7-9]. However, as the operation of conventional transistors is based on the modulation of the current flow in the device by an electrical field, there are critical challenges in maintaining good performance, reliability, and manufacturability when the device dimensions are reduced to the few-nanometre scale [10-12]. Surface states, heat dissipation, short-channel effects, and quantum confinement effects are some of the bottlenecks of conventional FET technology based on silicon and III-V semiconductors [13-17]. Searching for new materials and alternative computing paradigms, therefore, would be a solution to overcome these challenges for future electronics.

In a conventional metal–oxide–semiconductor FET, the current flow is switched on and off through the thermionic injection of electrons over a gate-tunable energy barrier. A gate voltage of at least 60 mV is required to increase the current by one order of magnitude at room temperature [18]. This value is typically termed Boltzmann's tyranny [19].

Quantum devices, including tunnel FET (TFET) [18, 20], topological transistors [19, 21], and superconducting transistors [22, 23], are predicted to overcome Boltzmann's tyranny. In TFETs, current flows *via* quantum tunnelling through a barrier rather than thermionic emission, allowing the achievement of a subthreshold slope below 60 mV/decade, which in principle can be as low as zero [18, 20, 24]. In addition, TFETs have much lower leakage currents because of their steep subthreshold slope and the fact that the tunnelling mechanism is more controllable at low voltages, resulting in remarkable power savings. Topological/superconducting transistors rely on electrically controlled quantum phase transitions in topological insulators or superconductors. Because spin and charge transport can occur without dissipation in the conducting channel, the device performance is limited only by the power dissipated when switching the transistor on and off. This process is theoretically predicted to be energy efficient compared to that of a conventional MOSFET [19, 25-27].

In a classical computer, FETs act as building blocks with ON and OFF states representing binary information (1s and 0s), allowing the execution of logical operations necessary to perform calculations. Quantum computing is a cutting-edge field that leverages the principles of quantum mechanics to process information in fundamentally different ways [28-30]. The basic unit of quantum information is a qubit, which can represent both 0 and 1 at the same time due to superposition. This allows different computational tasks to be performed simultaneously, which, for some computation tasks, leads to an exponential speed increase. Quantum computers are expected to produce solutions to complex problems which cannot be solved by classical computers or that demand extreme amounts of computational and energy resources. Among numerous qubit implementations, topological qubits are predicted to be more stable and inherently robust compared to popular approaches based on elementary particles such as trapped ions and single photons/electrons/spins [31-34]. Topological qubits are thus promising candidates for building large-scale quantum computers that are less susceptible to noise errors and therefore have higher error resistance. Experimentally, topological qubits can be realised in topological superconducting structures by placing a conventional superconductor in proximity to a material with strong spin-orbit coupling, such as topological insulators, semiconductor nanowires, or chains of magnetic atoms chains [35-37].

Tremendous efforts and resources from both academia and mainstream technology companies are spent on searching for innovation for post-Moore era electronics [38, 39]. TFETs, topological insulators, and topological qubits have been realised in epitaxially grown heterostructures made of conventional semiconductors and superconductors, such as silicon and III-V compounds [40-42]. However, fabricating high-quality nanostructures without defects and dislocations at the surfaces and interfaces of these materials *via* epitaxial growth is a great challenge. Even for near-perfect heterostructure interfaces, quantum effects are rarely observed at high temperatures (above 77 K), which severely limits their practical applications [43, 44].

Two-dimensional (2D) layered materials and their heterostructures, the so-called van der Waals (vdW) heterostructures, have drawn extensive attention recently owing to the intriguing possibility of engineering heterostructures with atomic precision without concern for lattice mismatch and interface disorder, as well as their possible use in future electronic components [45-47], circuits [48], and architectures [49]. 2D materials are atomically thin and offer a smooth channel-to-dielectric interface without dangling bonds. Relatively high carrier mobilities combined with low

leakage currents can be achieved even for channel thicknesses below one nanometer, which are unable to achieve in Si-based devices [49, 50]. Moreover, 2D materials can be stacked on arbitrary substrate or made freestanding. This offers the possibility of monolithic 3D integration [51]. Importantly, in 2D materials and vdW heterostructures, sharp interfaces, strong Coulomb interactions, and/or spin-orbit coupling permit observations of various quantum phenomena even at room temperature [52-56].

In this article, we review recent progress in the interface engineering of vdW heterostructures to realise high-temperature quantum effects based on interlayer tunnelling and the coupling of charged carriers and spins for energy-efficient devices, including TFETs, topological/superconducting transistors, and quantum computers. Interface engineering is defined as i) selecting 2D components appropriate for the target heterostructure and of sufficient quality, ii) stacking them at right angles, and iii) maintaining clean and sharp interfaces to maximise interlayer coupling and reduce detrimental scattering effects. The studied emergent phenomena include quantum tunneling, Josephson tunneling, exciton condensation, and topological superconductivity, as depicted in Fig. 1. In section 2, we discuss the phenomenon of negative differential resistance, which originates from the band-to-band tunnelling of single electrons/holes in vdW heterostructures. This is the mechanism behind the operating principle of the TFET. Quantum tunnelling through a thin barrier also occurs with paired particles, as in the case of superconducting junctions, known as Josephson tunnelling. Josephson junctions (JJs) have important applications for superconducting quantum interference devices (SQUIDs), superconducting transistors, and quantum circuits [57-61]. JJs built from vdW heterostructures are addressed in section 3. Under certain conditions, the bound pairs of electrons and holes between two separated 2D layers form a macroscopic quantum state of Bose-Einstein condensation (BEC), akin to Cooper pairs in superconductors [62, 63]. The condensation of excitons has been explored as a potential avenue for achieving high-temperature superfluidity and superconductivity [63-66]. We present the recent processes in searching for room-temperature exciton BEC in vdW heterostructures in section 4. In section 5 we review high-temperature quantum spin Hall effects in 2D materials and their potential applications for topological transistors and spin FETs. Topological superconductivity in 2D materials and vdW heterostructures, which may host Majorana modes for topological quantum computing is discussed in section 6. Several theoretically proposed structures for seeking high-temperature Majorana zero modes in vdW heterostructures

are also addressed in this section. Finally, in the last section, we summarise current state of the art and offer perspectives for the research field looking forward.

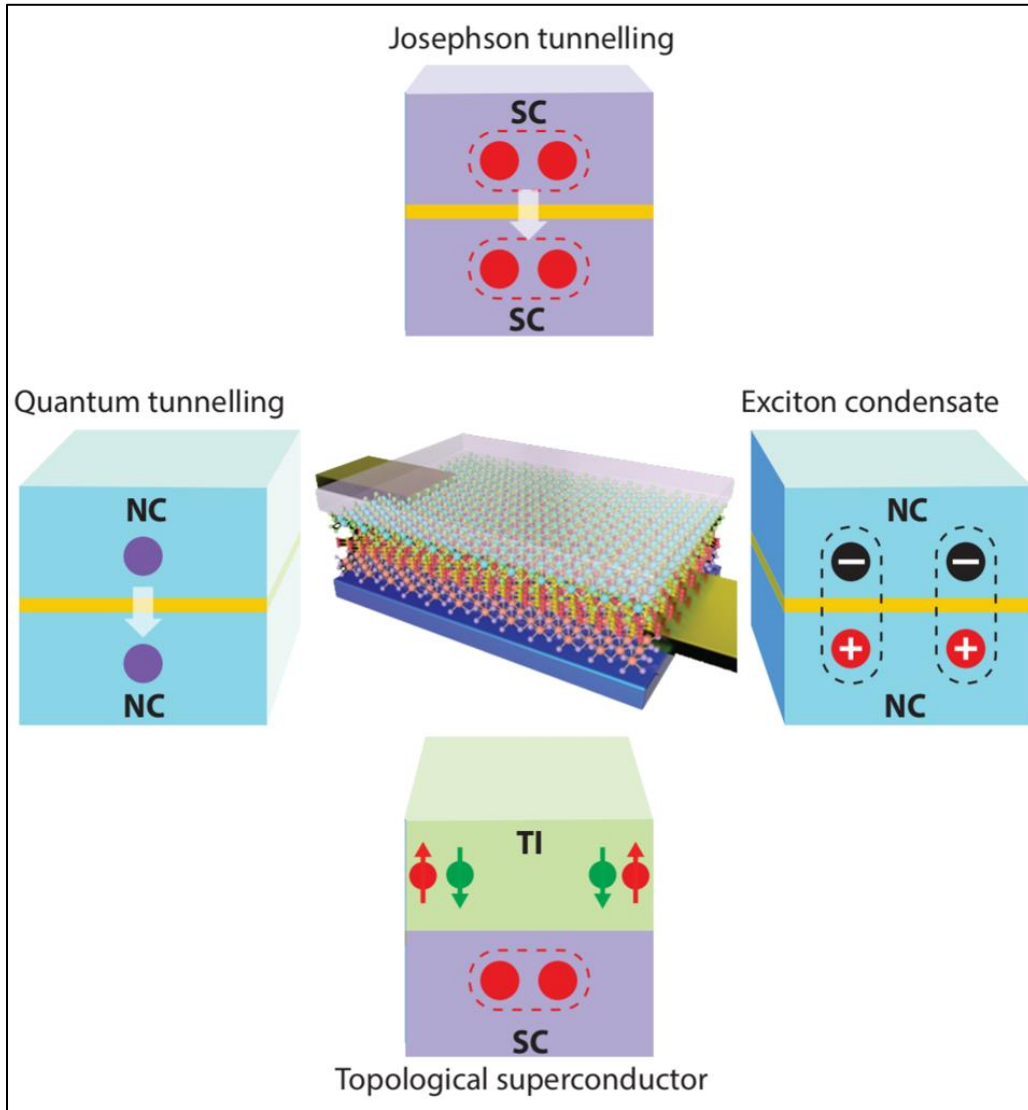


**Figure 1. Emergent phenomena in vdW heterostructures due to interlayer tunnelling and the coupling of charged carriers and spins including quantum tunnelling, Josephson tunnelling, exciton condensate, and topological superconductivity.** These are the underlying mechanisms for energy-efficient devices such as tunnel field-effect transistors, topological/superconducting transistors, high-temperature superconducting devices, and quantum computers. The center panel illustrates a typical device with two conducting monolayers separated by a few layers of an insulator. Two gold electrodes are used to inject charge carriers into the top and bottom conducting layers. NC: normal conductor (semiconductor, semimetal), SC: superconductor, TI: topological insulator.

## 2. Negative differential resistance and tunnel field-effect transistor

The current-switching process of an FET is characterized by a parameter called the subthreshold swing (SS), which is defined as  $SS = \frac{\partial V_G}{\partial \Psi} \frac{\partial \Psi}{\partial (\log_{10} I_D)}$ , where  $V_G$  is the gate voltage,  $I_D$  is the drain current, and  $\Psi$  is the surface potential of the semiconductor [18]. The first term is the transistor body factor and equals the unit in the ideal case, whereas the second term reflects the conduction mechanism in the channel. For conventional FETs based on thermionic injection, the minimum value of the second factor can be calculated as  $\frac{kT}{q} \ln 10$ , where  $k$ ,  $T$ , and  $q$  are the Boltzmann constant, temperature, electron charge, respectively, which has a value of 60 mV/dec at room temperature [18]. TFETs, where the current flow is governed by quantum-mechanical band-to-band tunnelling, would achieve an SS value lower than 60 meV (ref. 18, 20). Experimentally, SS can be extracted from the slope of the transfer curve ( $I_D$  vs.  $V_G$ ) in the subthreshold region [18]. TFETs offer not only a higher on/off ratio but also power savings with a smaller SS compared to those of other devices, including bulk silicon-based metal-oxide-semiconductor FETs and high-mobility FETs [18].

The heart of TFETs is an Esaki diode, where band-to-band tunnelling is manifested by a negative differential resistance (NDR) in the current-voltage curves of the device owing to the alignment of the energy bands of the junction [67]. Esaki diodes can be built from a heavily doped p-n junction, forming a narrow depletion region or broken-gap heterostructure with ultrathin tunnel barriers [67-69]. In the tunnelling regime, the current reaches a maximum value when the band edges of the junction are well aligned, and then decreases with increasing applied voltage, resulting in NDR behaviour.

Owing to the excellent band-edge modulation via gating in 2D materials, TFETs have been realised in numerous vdW heterostructures [70-78]. For example, by stacking bilayer MoS<sub>2</sub> on highly p-doped Ge, Sarkar *et al.* reported a TFET with a subthermionic subthreshold swing at room temperature [70]. Because the band alignments of the Ge-MoS<sub>2</sub> junction form a staggered heterostructure, the applied gate voltages modulate the band edges of MoS<sub>2</sub>, which in turn, controls the tunnelling current through the junction. Although the transfer curves of the fabricated devices show sub-60 mV SS, no clear NDR behaviour was observed in their I-V characteristics [70]. This is just an unusual slop region in the I-V curves, which the authors addressed as a trend toward

NDR, as MoS<sub>2</sub> is only slightly n-doped [70]. However, this may be because of the numerous defects formed in Ge/MoS<sub>2</sub> during the stacking process.

Interface quality is a critical factor in tunnel junctions. Defects at the interface can act as trap and/or recombination centres, leading to reduced tunnelling current [79, 80]. They may also induce pinning effects between band edges, resulting in junction blurring [81]. In vdW heterostructures fabricated by manual stacking processes, defects are commonly created at the interface during sampling in ambient conditions, regardless of using the so-called wet or dry transfer methods [82, 83]. These interfacial defects include bubbles of air, water vapour, and/or hydrocarbon residues trapped at the interface [84-86]. Creating a clean vdW heterostructure interface would be a route to achieving high-performance TFETs. Indeed, the junctions of WSe<sub>2</sub>/MoSe<sub>2</sub> and MoS<sub>2</sub>/WSe<sub>2</sub> synthesized by metal-organic chemical vapor deposition (MOCVD) exhibited robust NDR behavior at room temperature [75], as shown in Fig. 2a and 2b. While some progresses have been made in high-quality 2D crystals [87], the synthesis of large-scale vdW heterostructures with defect-free interfaces for device applications remains highly challenging [88-90]. By selecting 2D components to form a largely staggered junction, clear NDR characteristics can be observed in stacked vdW heterostructures [76]. For example, Fig. 2c and 2d show the structure and I-V curves of the SnSe<sub>2</sub>/black phosphorous (BP) heterostructure [76]. Using high-quality thin insulating layers, such as h-BN or Al<sub>2</sub>O<sub>3</sub>, inserted between the two 2D semiconducting layers may protect the junction sharpness, thereby enhancing the tunnelling current [77, 78] (Fig. 2e and 2f). Fabricating vdW in an inert environment also improves the NDR behaviour of the device [91, 92].

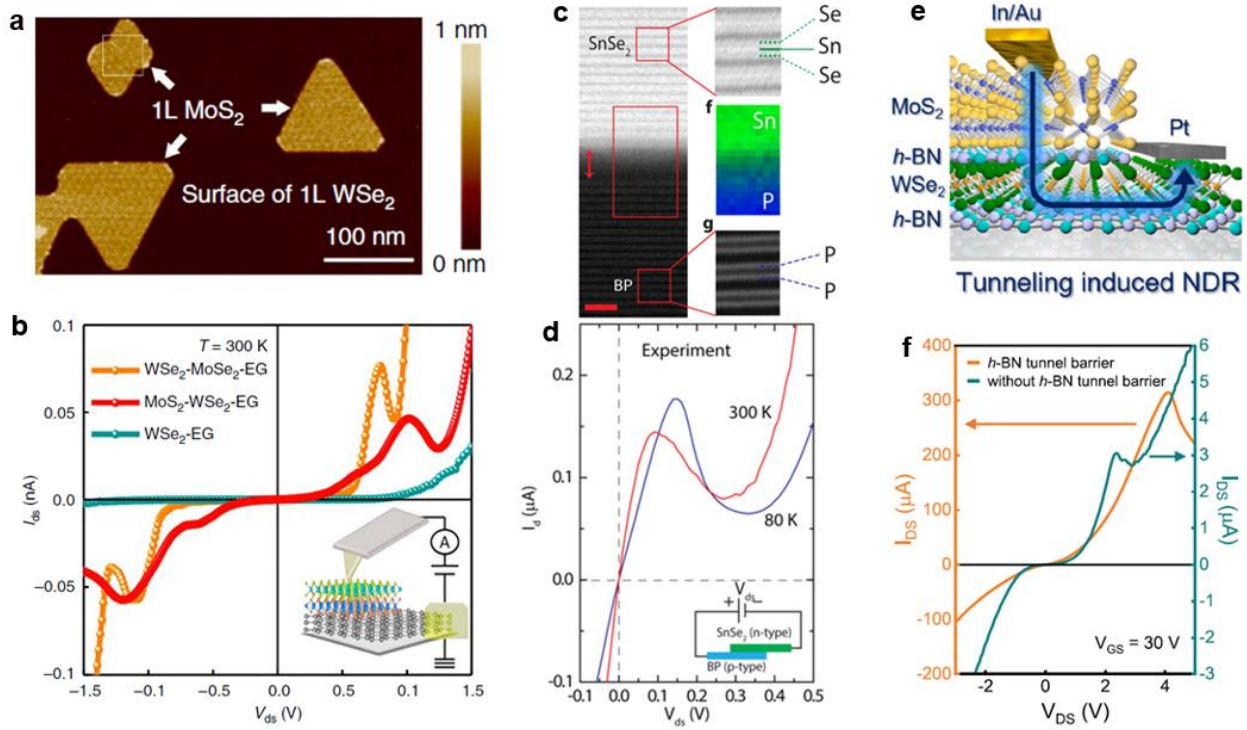


**Figure 2. Observation of negative differential resistance (NDR) at room temperature in vdW heterostructures.** (a, b) AFM image and I-V characteristics of synthetic MoS<sub>2</sub>/WSe<sub>2</sub> vdW heterostructures grown by metal-organic chemical vapour deposition (MOCVD). Synthetic vdW heterostructures offer clean interfaces, but are typically limited to small scales and few selected 2D components. EG: multilayer epitaxial graphene. (c, d) Cross-sectional TEM images and I-V characteristics at 80 and 300 K of stacked SnSe<sub>2</sub>/BP. BP: black phosphorus. A thin amorphous region formed at the interface during device processing acts a tunnelling barrier and maintains the broken-gap band alignment of the heterostructure for observation of the prominent NDR. Scale bar in (c) is 2 nm. (e, f) Device schematic and I-V characteristics of the stacked MoS<sub>2</sub>/hBN/WSe<sub>2</sub> heterostructures at room temperature. Insertion of thin insulating hBN layers (thickness of 3-4 nm) at the interface results in the formation of sharp band edges and an inelastic tunnelling current. NDR with a typically high peak current (315  $\mu$ A) is achieved at room temperature. Reprinted and adapted with permission: (a) and (b) from [75] (Springer Nature), (c) and (d) from [76] (ACS), (e) and (f) from [77] (ACS).

Van der Waals heterostructures made of ultrathin crystals from 2D materials can be used to build resonant tunneling devices, which have potential applications for the single-electron FET [93-99]. Graphene/hBN/graphene junctions are among the most frequently investigated vdW heterostructures for resonant tunneling and NDR devices, because they offer inert and clean interfaces [93, 94]. However, graphene is a gapless semiconductor, which limits the tunability of its gate modulation in TFETs. Building the channel part with 2D few-layer semiconductors, semiconducting vdW heterostructures, or moiré superlattices allows the generation of multiple energy levels for resonant tunnelling *via* layer number control, gate modulation, and twist angle

engineering [95-98]. Fig. 3 shows some examples of TFET with multiple NDR peaks based on few-layer crystals of InSe and WSe<sub>2</sub> [97, 98]. Observations of room-temperature resonant tunnelling in these vdW heterostructures provide an opportunity to build single-electron transistors for practical applications [99, 100].

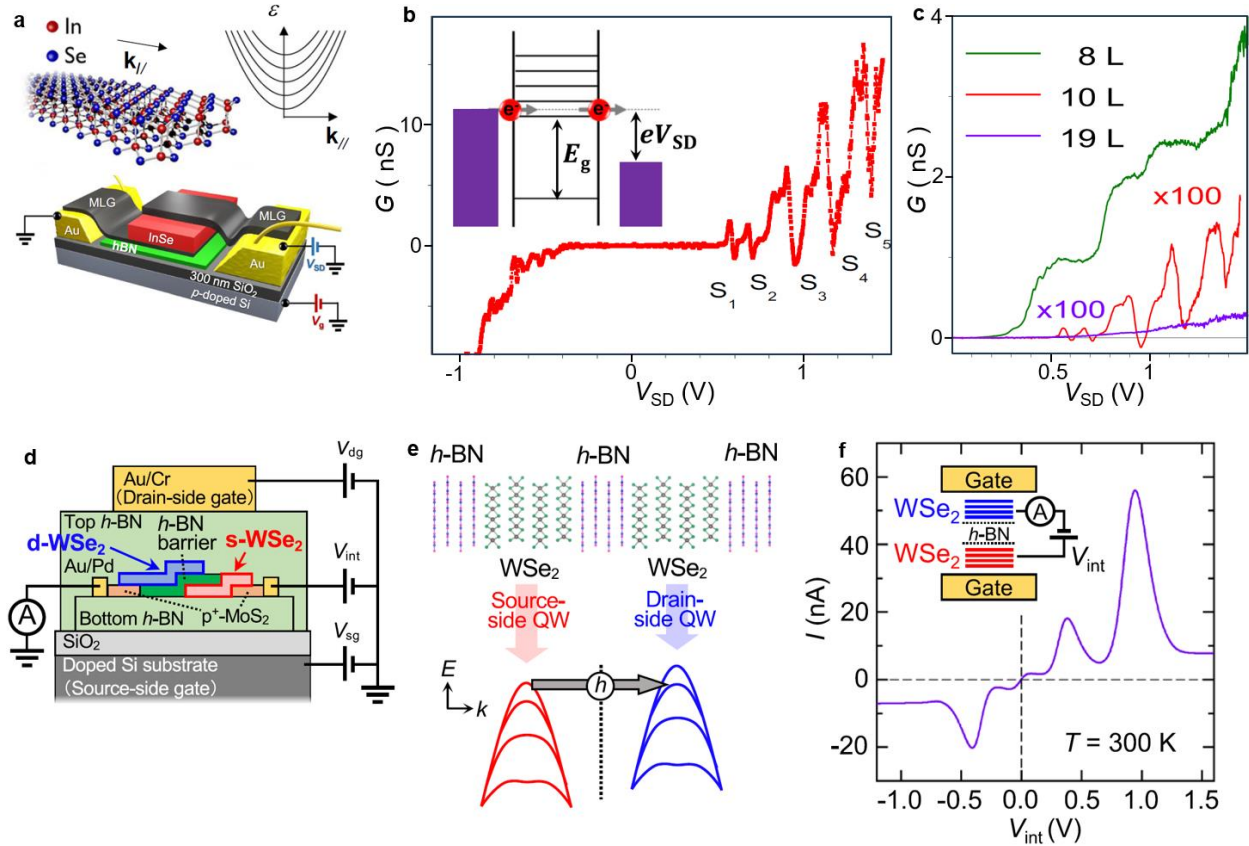


**Figure 3. Observation of resonant tunnelling into subbands of multilayer vdW materials.** (a) Crystal structure and device schematic for observation of resonant tunnelling in multilayer InSe. MLG: multilayer graphene. The energy of the 2D subbands can be tuned by varying the thickness of the InSe layer, owing to strong quantum confinement of the light-effective mass electrons. Resonant tunnelling occurs when the chemical potential in the source (MLG electrodes) is matched with a given 2D subband of InSe, leading to a peak in the I-V characteristics of the device. (b) Differential conductance curve,  $G$  vs.  $V_{SD}$ , at  $V_g = 0$  V and  $T = 2$  K for a device with ten-layer InSe. The inset shows the tunnelling of electrons from the MLG electrode (source) into the 2D subbands of InSe. (c) Differential conductance curves of devices with InSe thicknesses of 8, 10, and 19 layers at  $V_g = 0$  V and  $T = 2$  K. (d-f) Device schematic, band structures, and I-V curve at 300 K of the WSe<sub>2</sub>/hBN/WSe<sub>2</sub> vdW heterostructure. The few-layer p-doped WSe<sub>2</sub> (3-5 layers) source and drain act as the quantum well with quantised subbands for holes, while a thin hBN (3-6 layers) is inserted at the interface to be used as the tunnelling barrier. Multiple NDR peaks are observed in I-V curve at 300 K and  $V_{backgate} = -70$  V and  $V_{topgate} = -13.5$  V. Reprinted and adapted with permission, (a-c) from [97] (Springer Nature), (d-f) from [98] (ACS).

One of the great advantages of vdW heterostructures over conventional epitaxial heterostructures is that there are no dangling bonds at the interface. This offers the ability to control the twist angle between the layers during device fabrication, which strongly alters the interlayer tunneling [101-103]. Fig. 4 shows that the tunnelling current in a graphene/hBN/graphene structure changes significantly when the twist angle between the two graphene layers is adjusted even a fraction of a degree [102]. The NDR peaks vanish when the twist angle is larger than  $5^\circ$ . This is attributed to alignment of the Dirac cones between the top and bottom graphene layers [102]. In vdW heterostructures made of 2D semiconductors or semimetals with anisotropic conductivity, tunneling currents should also depend strongly on the twist angle due to the alignment/misalignment of the Fermi surfaces or Fermi arcs [103, 104]. For example, Srivastava *et al.* observed that the transport properties of stacked black phosphorus junctions transform from linear to tunnelling behavior when the twist angle is changed from  $0^\circ$  to  $90^\circ$  [ref. 103]. Therefore, attention should be paid to the twist angle during device processing to optimise the tunnelling current and NDR peaks.

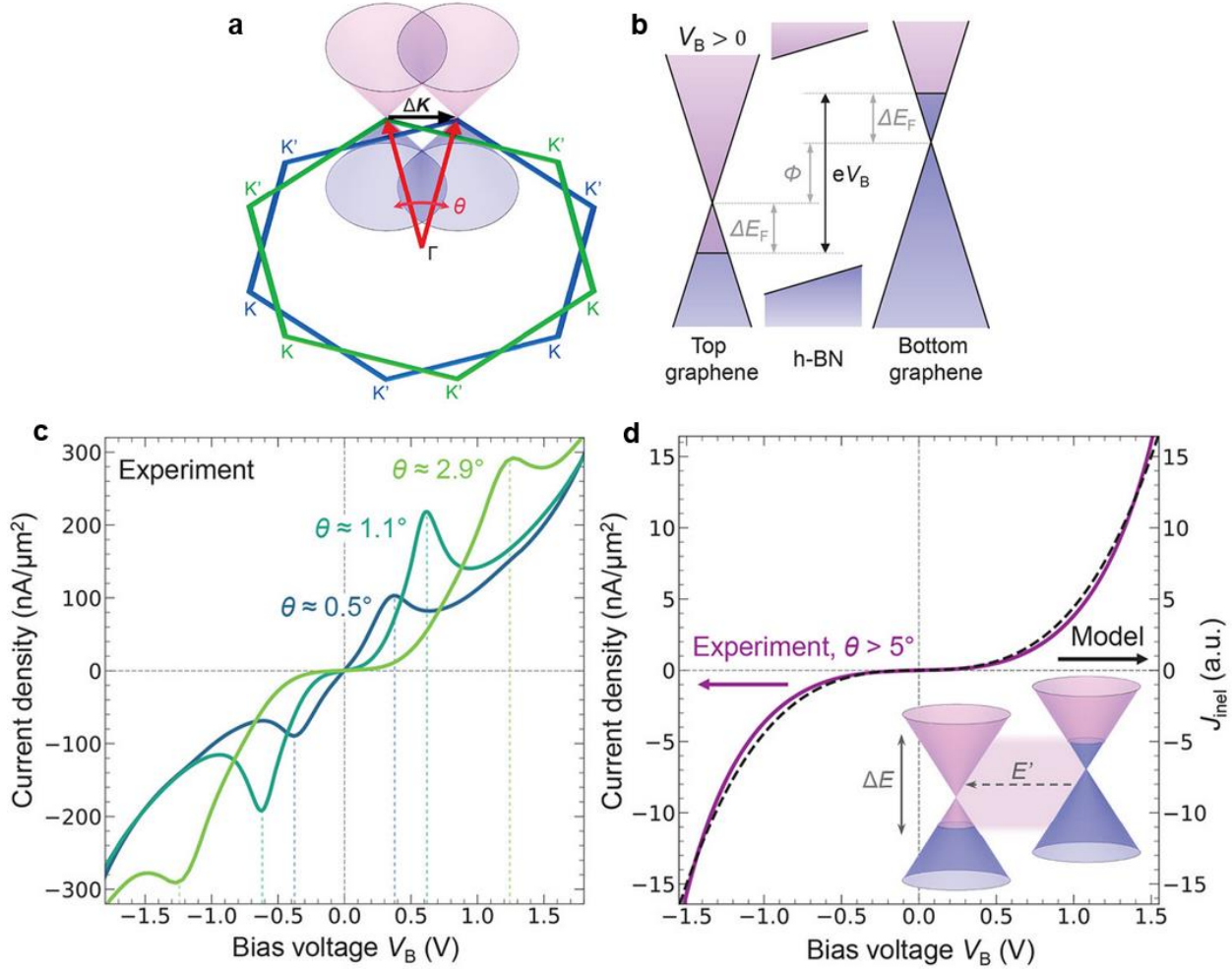


**Figure 4. Twist-angle dependence of resonant tunnelling in vdW heterostructures.** (a) Alignment of Brillouin zones of two graphene layers stacked at a twist angle of  $\theta$ . The twist angle translates into a wavevector mismatch  $\Delta K$  between the Dirac points of the top (green) and bottom (blue) graphene monolayers. (b) Energy band alignment of the Gr/hBN/Gr heterostructure under an applied bias between the top and bottom graphene layers. The applied voltage  $V_B$  introduces an energy offset  $\Phi$ , together with the Fermi level shift  $\Delta E_F$ . An increase in the twist angle enlarges the separation of the Dirac cones in momentum space and shifts the resonance condition to higher  $V_B$  values. For  $\theta \gtrsim 5^\circ$ , the momentum mismatch  $\Delta K$  becomes large, leading to vanishing tunnelling current peaks. (c, d) I-V characteristics of graphene/hBN/graphene tunneling devices with different twist angles. Reprinted and adapted with permission, (a-d) from [102] (ACS).

As the tunnelling current is strongly affected by defects at the interface and twist angles between the layers, a natural homojunction formed within vdW materials can offer a clean and well-aligned interface for achieving high-performance TFETs [105, 106]. Black phosphorous (BP) is a good candidate for this purpose because it is a semiconductor with high carrier mobility, a direct band gap even in the bulk form, and strongly thickness-dependent band edges [107]. Indeed, by making the device within the same flake of BP with different thicknesses between the monolayer and

multilayer regions, Kim *et al.* built a TFET with superior performance compared to those of the previous ones [108], as summarised in Fig. 5. Their TFETs show record-low average SS values ( $\sim 22.9 \text{ mV dec}^{-1}$ ) over 4 current decades with record-high on-current ( $I_{60} = 0.65 \mu\text{A } \mu\text{m}^{-1}$ ), which are promising for application in low-power switching devices [108]. However, BP is very sensitive to the oxygen environment; thus, passivation methods and/or special device processing should be developed to prevent device degradation for real applications [109-111].

Alternative methods have also been developed in recent years to achieve subthermionic-SS FETs such as negative-capacitance FETs [112-114], phase-transition FETs [115, 116], Dirac-source FETs [117-119], and junctionless NDR devices [120, 121]. However, while negative-capacitance and phase-transition FETs usually exhibit hysteresis in the switching process, others may require complicated device configurations with additional fabrication steps.

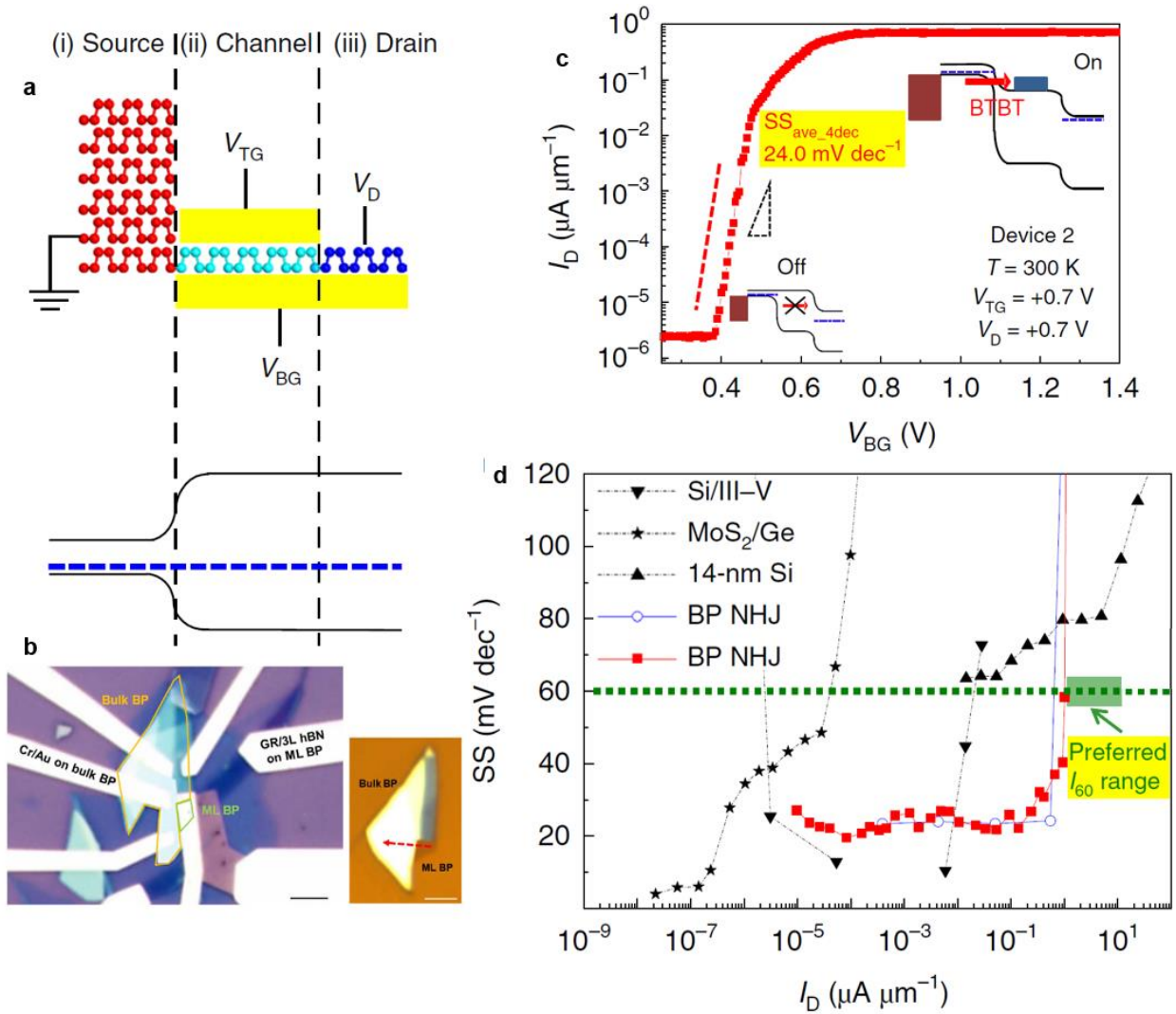


**Figure 5. Natural homojunction TFET.** (a) Schematic structure and band diagram of a TFET made of black phosphorus (BP) with different thickness regions between the bulk and monolayer within the same exfoliated flake. (b) Optical image of the BP tunnelling device. Graphene (GR) and 3-layer hBN are used as the back-gate and dielectric layer for monolayer BP (ML BP) region, respectively. (c) Transfer characteristics ( $I_D$  vs.  $V_G$ ) of device with bottom gate control. (d) Comparison of the subthreshold swing (SS) as a function of the ON current of the BP TFET with that of various FETs showing the achievement of sub-60 meV SS with a high ON current. Reprinted and adapted with permission, (a-d) from [108] (Springer Nature).

### 3. Josephson tunneling junctions and diodes

In superconductors electrons form Cooper pairs, that maintain quantum coherence over macroscopic distances and move through a material without resistance [122, 123]. When two superconductors are separated by a thin insulating layer, the Cooper pairs can tunnel through this barrier allowing a supercurrent to flow between the superconductors without any applied voltage, an effect called Josephson tunneling as it predicted in 1962 by Brian D. Josephson [124].

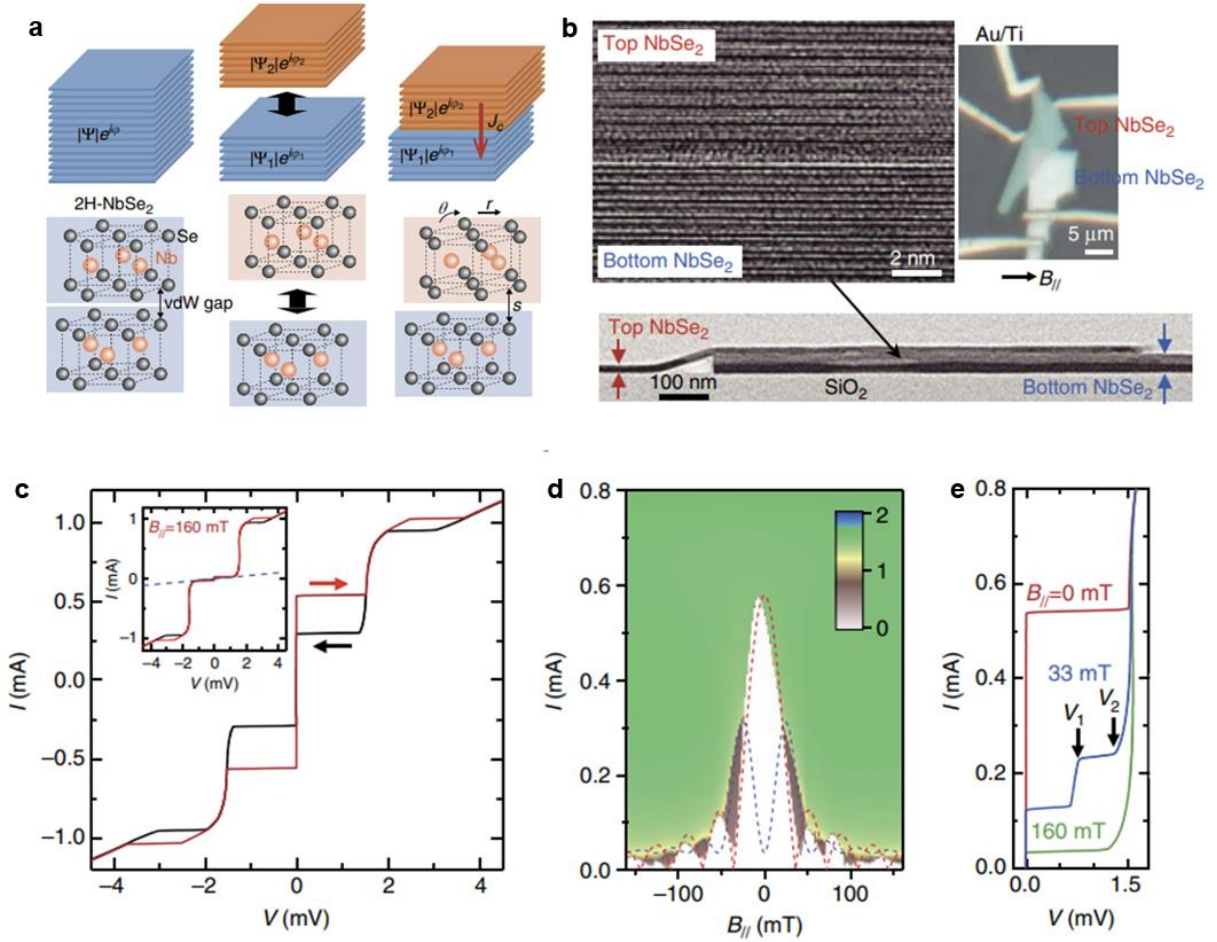


**Figure 6. vdW Josephson junction.** (a, b) Crystal structure and cross-sectional TEM images of the NbSe<sub>2</sub>/NbSe<sub>2</sub> junction. In the natural bulk form, the interconnected layers function as one superconductor with a single-order parameter  $|\Psi|e^{i\phi}$ . In stacked junctions, misalignment and misorientation of the layers and/or a larger vdW gap in the stacked junction induce interlayer decoupling and require different order parameters for each side of the vdW gap,  $|\Psi_1|e^{i\phi_1}$  and  $|\Psi_2|e^{i\phi_2}$ . (c) Electrical characteristics of the device showing the characteristics of the JJ with a large critical current of  $I_c = 0.53$  mA and hysteresis in the I–V curve. (d) Contour plot of  $V$  as a function of  $I$  and  $B_{||}$  at 2 K, showing the Fraunhofer pattern of JJ. The colour bar shows the value of  $V$  in mV. (e) I–V curves of the junction with applied in-plane  $B$ . Fiske resonances are observed as current steps at bias voltages  $V_1$  and  $V_2$  when  $B_{||} = 33$  mT. Reprinted and adapted with permission, (a–e) from [125] (Springer Nature).

A simple vdW JJ can be fabricated by stacking 2D superconductors, for example NbSe<sub>2</sub>, together even without an inserted insulating layer [125], as shown in Fig. 6. In the natural bulk form, the NbSe<sub>2</sub> multilayers have the same atomic arrangement, and the interconnected layers work as one superconductor with a single-order parameter,  $|\Psi|e^{i\phi}$ , as shown in Fig. 6a. Manually stacking the two layers together induces misalignment, misorientation, and/or a larger vdW gap (Fig. 6a). When the interlayer decoupling becomes sufficiently large, the superconducting state of the NbSe<sub>2</sub>

crystal created across the artificially connected vdW interface cannot be described by a single-order parameter but rather requires different order parameters for each side of the vdW gap,  $|\Psi_1|e^{i\varphi_1}$  and  $|\Psi_2|e^{i\varphi_2}$ . The flow of the supercurrent across the interface then follows the Josephson relation:  $I = I_c \sin(\varphi_1 - \varphi_2)$ , where  $I_c$  is the critical current [125]. Although there is a blurred region observed at the interface of the junction (Fig. 6b), possibly attributed to the stacking process being carried out under ambient conditions, the fabricated NbSe<sub>2</sub>/NbSe<sub>2</sub> device shows a large critical current of  $I_c = 0.53$  mA with hysteresis of the I–V curve, characteristics of the JJ (Fig. 6c). In addition, the Fraunhofer pattern and Fiske resonance are also observed in the magnetic field dependence of the I–V curve of the device (Fig. 6d and 6e), further confirming the properties of the JJ [125].

The atomic and tunable thickness of 2D materials with a broad conductivity range, from insulating to metallic and superconducting [126-128], allows us to choose various types of barriers for JJ to explore new tunnelling mechanisms and novel quantum devices [129-134, 137, 138]. For example, by inserting a monolayer ferromagnet, Cr<sub>2</sub>Ge<sub>2</sub>Te<sub>6</sub>, between superconducting NbSe<sub>2</sub>, Josephson tunnelling becomes spin-dependent and can be modulated by the magnetization direction of the barrier [132], as shown in Fig. 7a and 7 b. In NbSe<sub>2</sub>, two spin components of Cooper pairs remain localized predominantly inside each layer, ( $K \uparrow - K' \downarrow$  or  $K \downarrow - K' \uparrow$ , where  $K$  and  $K'$  denote the electronic band near the  $K$  and  $K'$  points) due to Ising Cooper pairing [132]. With perpendicular magnetization, Ising-Cooper pairs can tunnel via spin-dependent energy levels without a spin flip, whereas for in-plane magnetization, tunnelling occurs with a spin flip. These results may lead to new spin- and phase-controlled quantum electronic devices [135, 136]. Using three-layer Nb<sub>3</sub>Br<sub>8</sub> as the tunnel barrier, field-free superconducting diode behavior, where a supercurrent and a normal current flow in the opposite directions in the absence of an applied magnetic field, is observed in the NbSe<sub>2</sub>/Nb<sub>3</sub>Br<sub>8</sub>/NbSe<sub>2</sub> heterostructures [137], as shown in Fig. 7(c-e). Because the unit cell of Nb<sub>3</sub>Br<sub>8</sub> is composed of six layers of Nb-Br edge-sharing octahedra with inversion centres lying between adjacent layers, the inversion symmetry is preserved in the even-layer crystal but broken in the odd-layer structure [137]. The asymmetric I-V characteristic (non-reciprocal behaviour) of JJ is due to the breaking of inversion symmetry in the vdW heterostructure, which consists of three layers of Nb<sub>3</sub>Br<sub>8</sub> [137].

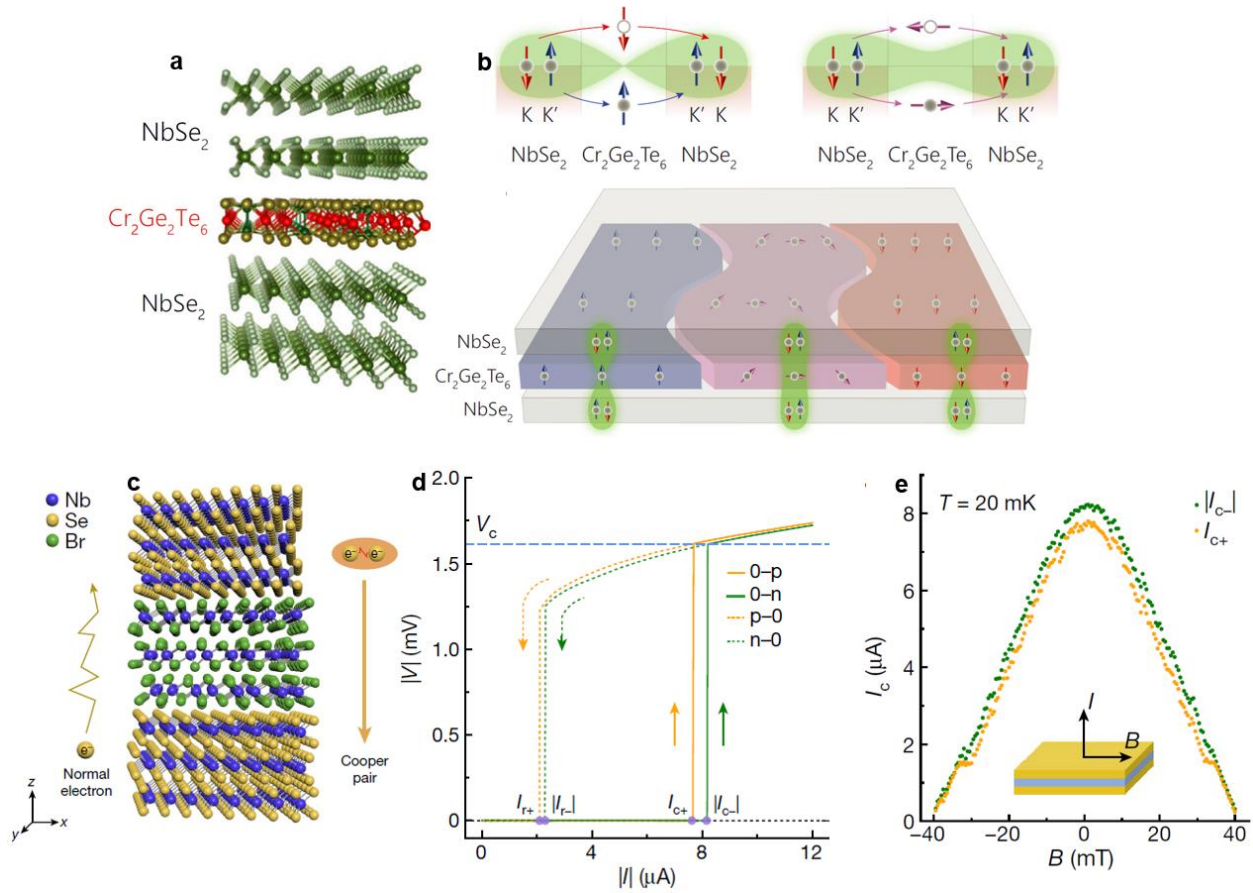


**Figure 7. Magnetic JJ and field-free vdW Josephson diodes.** (a, b) Crystal structure and spin-dependent tunnelling processes in the NbSe<sub>2</sub>/Cr<sub>2</sub>Ge<sub>2</sub>Te<sub>6</sub>/NbSe<sub>2</sub> JJ. NbSe<sub>2</sub> is a superconductor, while Cr<sub>2</sub>Ge<sub>2</sub>Te<sub>6</sub> is a magnetic insulator. Under perpendicular magnetisation, Ising-Cooper pairs can tunnel via spin-dependent energy levels without a spin flip, whereas for in-plane magnetisation, tunnelling occurs with a spin flip. (c-e) Crystal structure and electrical characteristics of the field-free Josephson diode made of NbSe<sub>2</sub>/Nb<sub>3</sub>Br<sub>8</sub>/NbSe<sub>2</sub> heterostructures. The supercurrent flows in one direction, whereas the normal current flows in the other direction because of the broken inversion symmetry of the vdW heterostructure owing to the odd layers of Nb<sub>3</sub>Br<sub>8</sub>. The measured I-V curve in (d), which contains four branches: sweeping the current from zero to positive (0-p), from positive back to zero (p-0), from zero to negative (0-n), and from negative back to zero (n-0), shows a large hysteresis with similar critical currents for the negative and positive regimes ( $I_{c+}$  vs.  $|I_{c-}|$  or  $I_{r+}$  vs.  $|I_{r-}|$ ). In panel (e)  $|I_{c-}|$ ,  $I_{c+}$  and  $|I_{c-}|$  are obtained from the 0-p and 0-n branches, respectively, while the magnetic field is swept from positive to negative in (e). The diode effect ‘turns off’ by  $\pm 35$  mT. Reprinted and adapted with permission, (a) and (b) from [132] (Springer Nature), (c-e) from [137] (Springer Nature).

The discovery of high-temperature superconductivity in monolayer Bi<sub>2</sub>Sr<sub>2</sub>CaCu<sub>2</sub>O<sub>8+δ</sub> (BSCCO) provides an ideal 2D quantum system for understanding unconventional superconductivity as well as for potential quantum devices operating above liquid nitrogen temperatures [139]. BSCCO is a member of the cuprate family and has been known for its high-temperature superconductivity since the 1980s. However, producing high-quality thin layers from its bulk form is extremely challenging owing to the sensitivity of their surfaces to the air environment. By developing sample

fabrication processes where BSCCO flakes are exfoliated on a cold stage kept at  $-40\text{ }^{\circ}\text{C}$  inside an Ar-filled glove box with water and oxygen content below 0.1 ppm, monolayer superconducting with  $T_c$  as high as that of the bulk form (88 – 90 K) is achieved, as shown in Fig. 8a. Importantly, the superconductivity of monolayer can be highly tunable by doping *via* annealing processes to modulate its oxygen concentration (Fig. 8b-c). This opens a great opportunity for the fabrication of electrically controlled superconducting devices such as Josephson diodes and transistors, quantum magnetometry, and quantum circuits [140-145]. Indeed, there have been recent studies reported about high-temperature Josephson diodes made of BSCCO stacked homojunctions [146] as well as gate-modulated superconductivity in thin BSCCO layers [147].

Importantly, Josephson tunnelling and diode behaviour are found to be sensitive to the stacking angles between the BSCCO layers [146], suggesting that twist angle engineering is an interesting and promising route for investigating novel quantum phenomena in these systems at high temperatures for practical applications, such as interferometers and quantum qubits [148, 149].

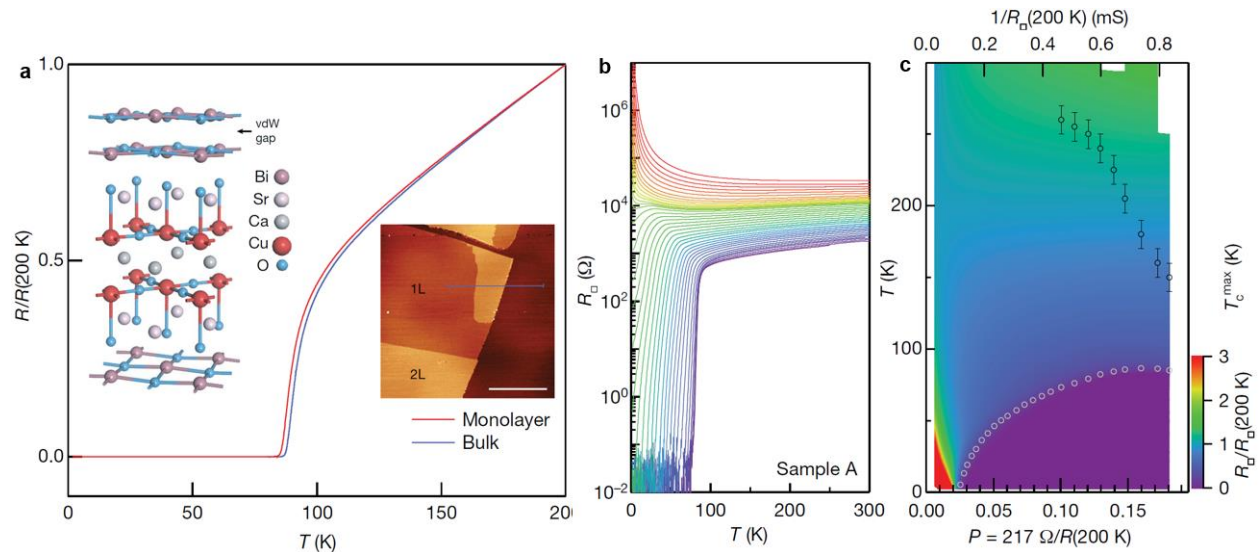


**Figure 8. Tunable high-temperature 2D superconductivity.** (a) Crystal structure and superconducting characteristics of  $\text{Bi}_2\text{Sr}_2\text{CaCu}_2\text{O}_{8+\delta}$  monolayers and bulk forms. Monolayer refers to a half unit cell in the out-of-plane direction that contains two  $\text{CuO}_2$  planes, separated by vdW gaps in bulk form (left inset). A high-quality intrinsic monolayer has  $T_c$  similar to that of the bulk form (88 K). Right inset: AFM image of monolayer and bilayer  $\text{Bi}_2\text{Sr}_2\text{CaCu}_2\text{O}_{8+\delta}$ . Scale bar is  $10\text{ }\mu\text{m}$ . (b) Temperature-dependent resistivity of a monolayer  $\text{Bi}_2\text{Sr}_2\text{CaCu}_2\text{O}_{8+\delta}$  with different initial doping levels  $p$  (holes per  $\text{CuO}_2$  plaque) *via* annealing from high (purple curves) to low (red curves). (c) 2D plot of the resistivity of the monolayer as a function of temperature and doping level. The doping level  $p$  is determined as  $p = 217\Omega/R_{\square}(T = 200\text{ K})$ . White circles indicate the superconducting transition temperature  $T_c$ . Reprinted and adapted with permission, (a-c) from [139] (Springer Nature).

Superconductivity and correlated insulators in magic-angle twisted bilayer graphene (MATBG) have been also studied extensively for JJs and superconducting interference quantum devices as they offer the flexibility and simplicity for fabricating high-quality JJ without edge disorder by electrostatic gating [150-155]. The conductivity of MATBG can be changed from insulating to superconducting *via* electrostatic gating [153]. By making the narrow gate electrodes for inducing superconducting regions separated by a short, non-superconducting weak link, a planar JJ can be created [155, 156]. However, the superconductivity and correlated states in MATBG have so far only been observed at very low temperatures (below 3 K) [157]. For many practical applications of JJ, 2D materials and vdW heterostructure architectures supporting high-temperature superconductivity must be identified. Recent observations of correlated states in twisted bilayer MoS<sub>2</sub> at room temperature seem encouraging [158].

#### **4. Exciton condensate and high-temperature superfluidity**

According to the BCS theory for superconductivity (SC), the critical temperature,  $T_c$ , at which Cooper pairs maintain quantum coherence, can never be higher than 30 K [ref. 159]. The discovery of SC in copper perovskites in the 1980s with a  $T_c$  above 130 K highlighted that the BCS theory does not cover all types of superconductors and all phenomena associated with superconductivity [160, 161].

An exciton is a particle-like entity that forms when an electron is bound to a positively charged “hole” through Coulomb interactions. While electrons and holes are fermions, the exciton is a boson, a particle with integer spin obeying the Bose-Einstein statistics [162]. Thus, excitons can condense into a collective quantum state known as an exciton condensate, which exhibits properties similar to Cooper pairs in superconductors [163, 164]. Because excitons have a light effective mass, it may be feasible to achieve Bose-Einstein condensation (BEC) at relatively low densities and accessible temperatures [165]. Although evidence of exciton BEC has been reported over the last few decades in epitaxially grown III-V semiconductor quantum wells, they only exist at very low temperatures and/or high magnetic fields because of the low binding energy and short lifetime of the excitons in these systems [166-170].

Room-temperature exciton condensation and superfluidity were theoretically predicted in graphene bilayers by Min *et al.* in 2008, as it is a gapless semiconductor with nearly perfect electron-hole symmetry and stiff phase order [171], as shown in Fig. 9a and 9b. The author

proposed a device structure in which two layers of graphene are separated by a dielectric medium with electron- and hole-doped top and bottom layers, respectively, by modulated double gates (Fig. 9a). The maximum possible Kosterlitz-Thouless temperature of the superfluids in the system is estimated to be above 300 K upon the distance between the two graphene layers and the external bias electric field (Fig. 9b). In 2017, with the discovery of high-quality and atomically thin insulating h-BN, Li *et al.* [172] and Liu *et al.* [173] independently fabricated devices with the same structure consisting of double bilayer graphene separated by a few-layer h-BN, which is very similar to the structure proposed by Min *et al.* Indeed, they observed the exciton condensate and superfluid phases in these structures, but only in the quantum Hall regime, where excitons are formed in a bilayer electron system under high magnetic field [172]. In this regime, the total number of electrons is less than the number of states in the lowest Landau level because a high magnetic field generates as many orbitals as the number of magnetic flux quanta. Owing to the particle-hole transformation, electrons occupy orbitals such that they always face empty orbitals (i.e. holes) in the opposite layer, leading to the formation of interlayer excitons [172, 173]. Evidence of exciton condensation is manifested by quantised Hall drag and dissipationless transport in the counterflow geometry [172]. Although the exciton condensation in these double bilayer graphene structures was robust and observed at a temperature ten times higher than that in a GaAs-based electron double layer [173], the requirement of a high applied magnetic field limits their practical application.

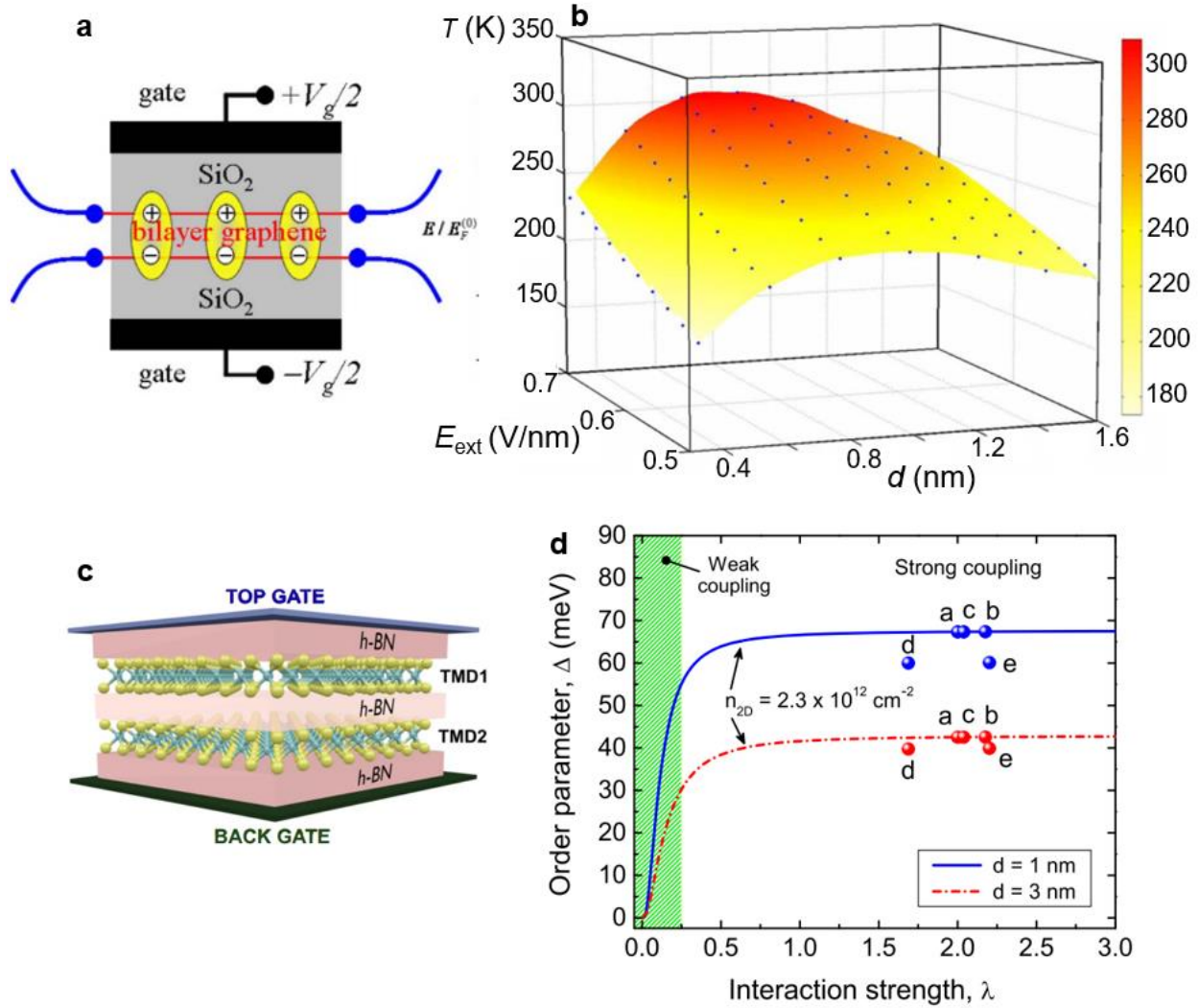


**Figure 9. Proposed vdW heterostructures for room-temperature exciton condensation and superfluidity.** (a) Two graphene layers are separated by a thin dielectric spacer while the electric field between the layers are controlled by the top and bottom gates. When the gate voltages are equal but have opposite signs ( $+V_g/2$  and  $-V_g/2$ ), the particle-hole symmetry of the Dirac equation ensures perfect nesting between the electron Fermi spheres in the n-type layer and its hole counterparts in the opposite layer, driving the Cooper instability for superfluidity. (b) Calculated superfluid phase diagram showing the dependence of the critical temperature  $T_c$  as function of the distance,  $d$ , and external bias field,  $E_{ext}$ , between the graphene layers. (c) Two monolayers of transition metal dichalcogenides (TMD) are separated by a thin insulating film of hBN. Using the double gate structure, the top and bottom layers are tuned to equal electron and hole density, respectively. (d) Calculated order parameter showing that room-temperature exciton condensation ( $\Delta > 25$  meV) can be achieved in the strong coupling regime ( $\lambda > 0.2$ , where  $\lambda$  is the ratio of the interaction energy to the band energy).  $d$  (1 and 3 nm) is the distance between the two TMD layers; the spheres (red and blue colors marked a, b, c, d, e) represent the calculated results for five vdW structures including MoTe<sub>2</sub>/MoS<sub>2</sub>, MoTe<sub>2</sub>/MoTe<sub>2</sub>, MoTe<sub>2</sub>/MoSe<sub>2</sub>, MoSe<sub>2</sub>/WSe<sub>2</sub>, and MoSe<sub>2</sub>/MoSe<sub>2</sub>, respectively. Reprinted and adapted with permission, (a) and (b) from [171] (APS), (c) and (d) from [183] (APS).

Semiconducting transition metal dichalcogenides (TMDs) have excitons with long lifetimes and high binding energy; and should therefore be promising platforms for high-temperature exciton condensates in vdW heterostructures [174-183]. The exciton binding energies in monolayer TMDs are in the range of hundreds of meV [ref. 174, 177]. Long-lived interlayer excitons with lifetimes of a few nanoseconds, an order of magnitude longer than the intralayer excitons in the monolayers, have been observed in MoSe<sub>2</sub>/WSe<sub>2</sub> vdW heterostructures without spacer layers [186]. Therefore, room-temperature exciton condensates have been predicted to exist in vdW heterostructures with semiconducting TMD monolayers separated by an insulating hBN spacer layer [183], as shown in Fig. 9c and 9d. The calculation of the order parameter ( $\Delta$ ) for several vdW hetero- and homostructures, including MoTe<sub>2</sub>/MoS<sub>2</sub>, MoTe<sub>2</sub>/MoTe<sub>2</sub>, MoTe<sub>2</sub>/MoSe<sub>2</sub>, MoSe<sub>2</sub>/WSe<sub>2</sub>, and MoSe<sub>2</sub>/MoSe<sub>2</sub>, shows that room-temperature exciton condensation ( $\Delta > 25$  meV) can be achieved in the strong coupling regime ( $\lambda > 0.2$ , here  $\lambda$  is the ratio of the interaction energy to the band energy) when the two TMD monolayers are separated by few-layer hBN (1-3 nm) (Fig. 9d) with an exciton density  $n_{2D} = 2.3 \times 10^{12}$  cm<sup>-2</sup>. In principle all these parameters are achievable in experiments.

In fact, the strong interlayer coupling in TMD vdW heterostructures has been observed experimentally. For example, the interlayer exciton emission, where electrons in MoS<sub>2</sub> monolayer recombine with holes in WSe<sub>2</sub> layers, is still observed even with the insertion of three layers of hBN between the two monolayers [177], as shown in Fig. 10a and 10b. Interestingly, by fabricating MoSe<sub>2</sub>/hBN/WSe<sub>2</sub> heterostructure device where the electron and hole densities in the MoSe<sub>2</sub> and WSe<sub>2</sub> monolayers are controlled *via* gate voltages and interlayer bias, as shown in Fig. 10c, Wang *et al.* indeed observed evidence of high-temperature exciton condensation surviving up to 100 K [184]. While luminescence of interlayer excitons is enhanced with a narrow peak at equal electron and hole densities, the interlayer tunnelling current depends only on the exciton density, manifesting correlated electron-hole pair tunnelling (Fig. 10d-f). The critical temperatures ( $T_c$ ) of the observed phenomenon above 100 K are consistent with the predicted exciton condensation in TMD vdW heterostructures, suggesting that it would be possible to improve  $T_c$  to approach room temperature by further optimising the device structures [183, 184].

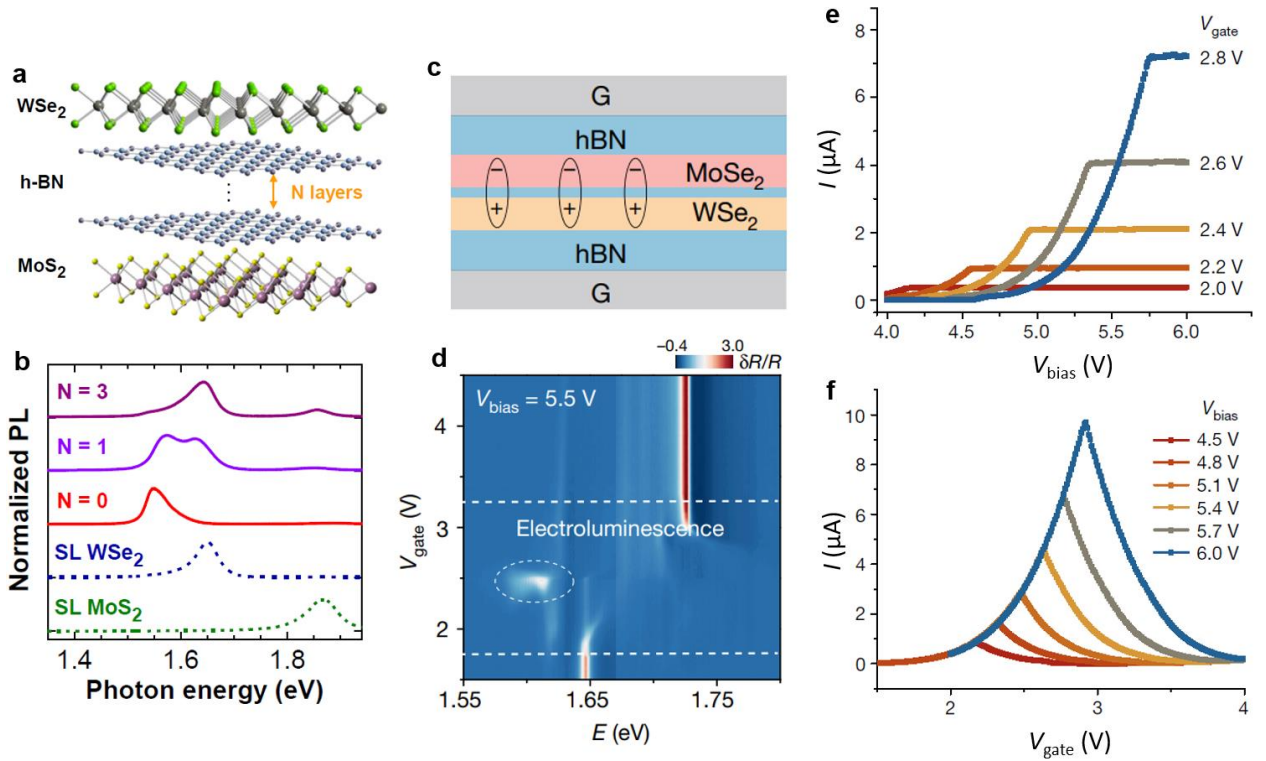


**Figure 10. Evidence of high-temperature exciton condensation in TMD-based heterostructures.** (a, b) Crystal structure and photoluminescence of MoS<sub>2</sub>/WSe<sub>2</sub> with the insertion of a thin hBN insulator at the interface. The lower-energy emission peak (in red curve) from interlayer excitons formed by electrons in the MoS<sub>2</sub> monolayer and holes in the WSe<sub>2</sub> monolayer. Interlayer exciton emission is observed even with the insertion of three layers of hBN indicating strong interlayer coupling. (e-f) Device structure, electroluminescence, and electrical characteristics showing correlated electron-hole pair tunnelling, a signature of exciton condensation, in the MoSe<sub>2</sub>/hBN/WSe<sub>2</sub> heterostructure. MoSe<sub>2</sub> and WSe<sub>2</sub> monolayers are separated by three-layer hBN. Few-layer graphene top and bottom gates (G) are used to tune the hole and electron densities in the WSe<sub>2</sub> and MoSe<sub>2</sub> layers, respectively. Electroluminescence of interlayer excitons is observed from the tunnel junction when  $V_{\text{bias}} = 5.5$  V is applied between the WSe<sub>2</sub> and MoSe<sub>2</sub> layers, and equal gate voltages ( $V_{\text{gate}}$ ) are swept (circled bright spot in (d)). The tunnelling current depends only on the electron-hole pair density, but not on the individual electron and hole densities, and has a maximum value at the charge balance ( $n = p$ ), manifesting the correlated tunnelling behaviour (shown in (e) and (f)). At a fixed  $V_{\text{gate}}$ , the current increases with increasing  $V_{\text{bias}}$  and reaches a constant value at the charge balance because the density of  $(n + p)$  unchanges. Similarly, the gate-dependent tunnelling current shows a cusp-shaped peak centred at the charge balance. The phenomena are consistent with the predicted exciton condensation, and persist up to 100 K. Reprinted and adapted with permission, (a) and (b) from [177] (NAS), (c-f) from [184] (Springer Nature).

As previously mentioned, vdW heterostructures fabricated by manually stacking are commonly plagued by defects at the interfaces and angular misalignments between the layers [81-86, 102]. These imperfections weaken the interlayer coupling and thus alter the exciton lifetime and binding energy, similar to the case of interlayer tunnelling, as discussed in Section 2. Numerous studies have shown strong dependences of interlayer coupling and exciton lifetime on twist angle in TMD

vdW heterostructures [185-190]. Moreover, electrons and holes located in different types of TMD layers may also induce a momentum mismatch between them leading to reduced interlayer coupling [191]. Therefore, using a natural homojunction formed within the same vdW material should, in principle, enhance the interlayer electron-hole pairing, as it provides a very clean interface structure with precisely aligned layers. We proposed a simple device architecture to search for high-temperature exciton condensates in naturally formed homojunctions within monolithic multilayer vdW crystals [192], as shown in Fig. 11. In unintentionally doped vdW layered materials, the conducting channels are spatially confined within their surface layers, while the inner layers remain intrinsic [193-197]. This allows us to build a double quantum well structure vertically within the crystal without the insertion of insulating layers [198, 199]. The spontaneously forming insulating region can be as narrow as a few nanometers in multilayer WSe<sub>2</sub>, but can be tuned by the gate voltage and/or temperature [199]. By introducing holes and electrons in the top and bottom layers simultaneously by application of gate voltages, zero-bias peaks were observed in the differential conductance curves of the device at room temperature as a signature of electron-hole pairing when their densities balance (Fig. 11d). The magnitude of the conductance peak is gradually reduced under the application of a magnetic field (Fig. 11e) as it weakens the phase coherence [199-201]. Our structure closely resembles the electrical reservoir for excitons, proposed by Xie and MacDonald [202], although the inserted h-BN insulating layers are replaced with the intrinsic WSe<sub>2</sub> bulk acting as a separator. Correlated electron-hole pair tunnelling occurs because the high work function of Au (5 eV) induces a tunneling barrier for electrons injected from the source to the n-doped WSe<sub>2</sub> bottom layers, whereas holes tunnel from the drain to the p-doped WSe<sub>2</sub> top layers through the intrinsic central region.

Correlated electron-hole pair tunnelling has been previously observed as strongly enhanced coherence interlayer tunnelling between stacked graphene layers through h-BN barriers at temperatures below 10 K [203, 204]. Our observations at 300 K in multilayer crystals of WSe<sub>2</sub> open a new opportunity for the realisation of room-temperature superfluidity in vdW materials using a simple, clean, and scalable approach as large-scale multilayer 2D materials can be grown by several methods, such as CVD, PLD, or MOCVD [205-207].

Exploring novel device configurations and exotic quantum material systems is also promising for achieving high-temperature exciton condensation. For example, embedding vdW heterostructures in a cavity to induce exciton polaritons may significantly enhance  $T_c$  because

exciton polaritons have a much lighter effective mass [208-210]. High-temperature vdW topological insulators could also provide a suitable platform because they have well-defined surface states and insulating bulk [211-215]. Hybrid structures of 2D materials with organic or perovskite semiconductors can offer strong interlayer coupling [216-219]. Finally, moiré superlattices of vdW materials possess unique characteristics for interlayer excitons owing to the strong localisation and correlation of electrons and holes [220-225].

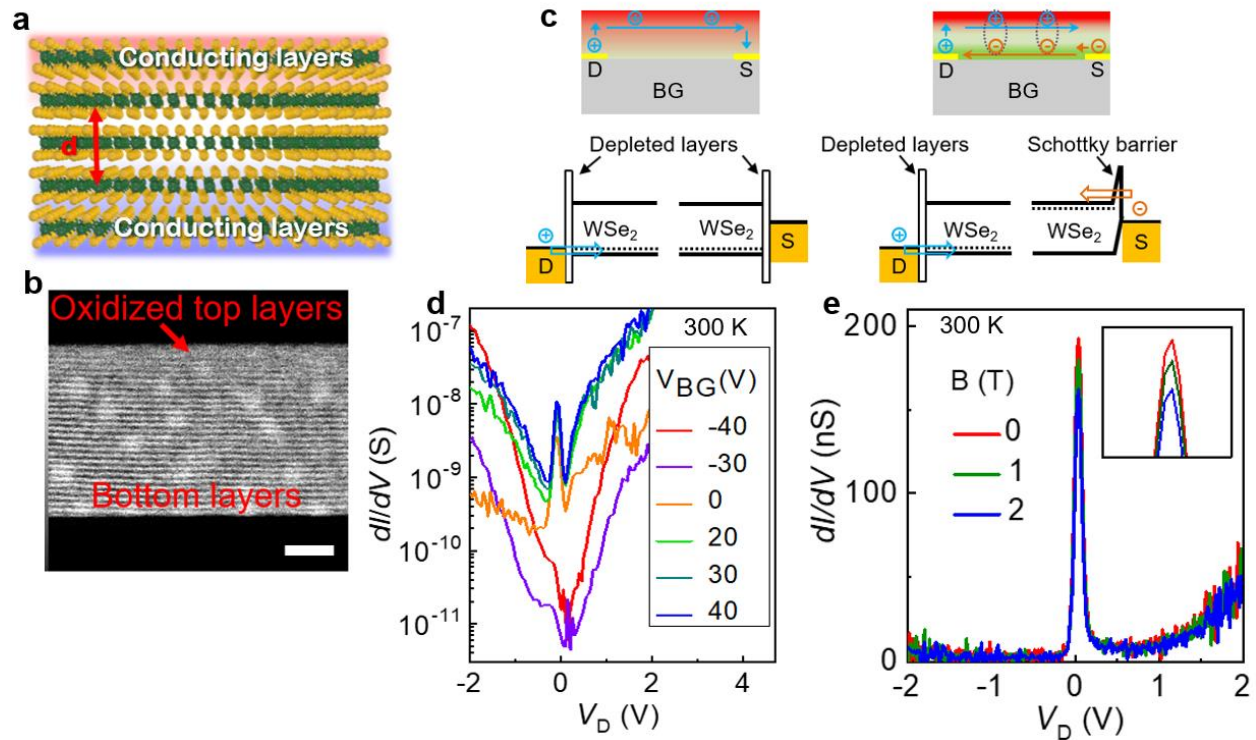


**Figure 11. Room-temperature correlated electron–hole pair tunnelling in multilayer vdW materials.** (a, b) Atomic model and cross-sectional TEM image of multilayer WSe<sub>2</sub>. The top and bottom conducting layers are separated by central intrinsic insulating layers of width  $d$ . Topmost layers are unintentionally p-doped because of oxidization, whereas bottom layers could be modulated by an electrostatic back-gate. (c-e) Device configuration, band diagrams, and electrical characteristics of multilayer WSe<sub>2</sub> device with Au bottom contacts. Under an applied bias, electrons and holes tunnel into the conducting top and bottom through barriers at the Au/WSe<sub>2</sub> interfaces. Zero-bias peaks are observed in the differential conductance curves of the device only when both electrons and holes exist (positive  $V_{BG}$ ), manifesting a signature of electron-hole pairing when their densities balance (Fig. d). The magnitude of the conductance peak is gradually reduced under the application of a magnetic field as it weakens the phase coherence (Fig. e). Reprinted and adapted with permission, (a) and (b) from [199] (Wiley), (c-e) from [192] (AIP).

## 5. Quantum spin Hall insulator and topological transistor

In normal (trivial) semiconductors or insulators, the valence and conduction bands are strictly separated by an electronic bandgap. In certain systems, the orbital structure of the crystal lattices induces an inversion of the conduction and valence electron bands, known as an inverted gap [35]. This band inversion combined with spin-orbit coupling (SOC) gives rise to the quantum spin Hall (QSH) effect, where the system has quantised spin-Hall conductance of  $e^2/h$  per one helical conducting edge and vanishing charge-Hall conductance [226]. These systems are called quantum spin Hall insulators, or topological insulators [226].

Graphene was early predicted to be a 2D QSH insulator in 2005 by Kane and Mele [227]. It was later found that the gap opened by weak SOC in graphene is very small, on the order of  $10^{-3}$  meV, making it unrealistic to realise experimentally [228]. The first robust QSH effect was experimentally observed in the HgTe/CdTe quantum wells in 2007 by König *et al.* [229]. Despite tremendous effort in searching for QSH insulators both theoretically and experimentally, conventional epitaxially grown materials and heterostructures and other systems such as Bi-based compounds usually have small inverted gaps of a few tens of meV, limiting the QSH states to exist at low temperatures [228-232].

Monolayer TMDs in 1T'-phase structure were proposed to host QSH states at high temperatures as it could open an inverted gap in a range of hundreds of meV as presented in Fig. 12 [233]. MX<sub>2</sub> TMDs (with M = W, Mo, and X = Te, Se, and S) exist in a variety of polytypic phase structures, including 1H, 1T, and 1T' (Fig. 12a). While 1H-MX<sub>2</sub> monolayers are normal semiconductors with direct bandgaps, their 1T phase is typically unstable under free-standing conditions and undergoes a spontaneous lattice distortion to convert into the 1T' structure possessing a set of quite different and unusual properties [234-237]. Using many-body perturbation theory calculations, Qian *et al.* [233] show that the structural distortion causes an intrinsic band inversion between chalcogenide-p and metal-d bands, opening an inverted gap up to 0.6 eV in 1T'-MoS<sub>2</sub> (Fig. 12b and 12c). Interestingly, this inverted gap can be modulated by an electrical field and/or strain, allowing creation of a so-called topological transistor with the possibility fast switching processes with low energy by modulation of the QSH states in the device (Fig. 12d and 12e) [233]. Robust QSH edge states are also predicted to appear at the phase boundary in various homo/heterostructures [238, 239].

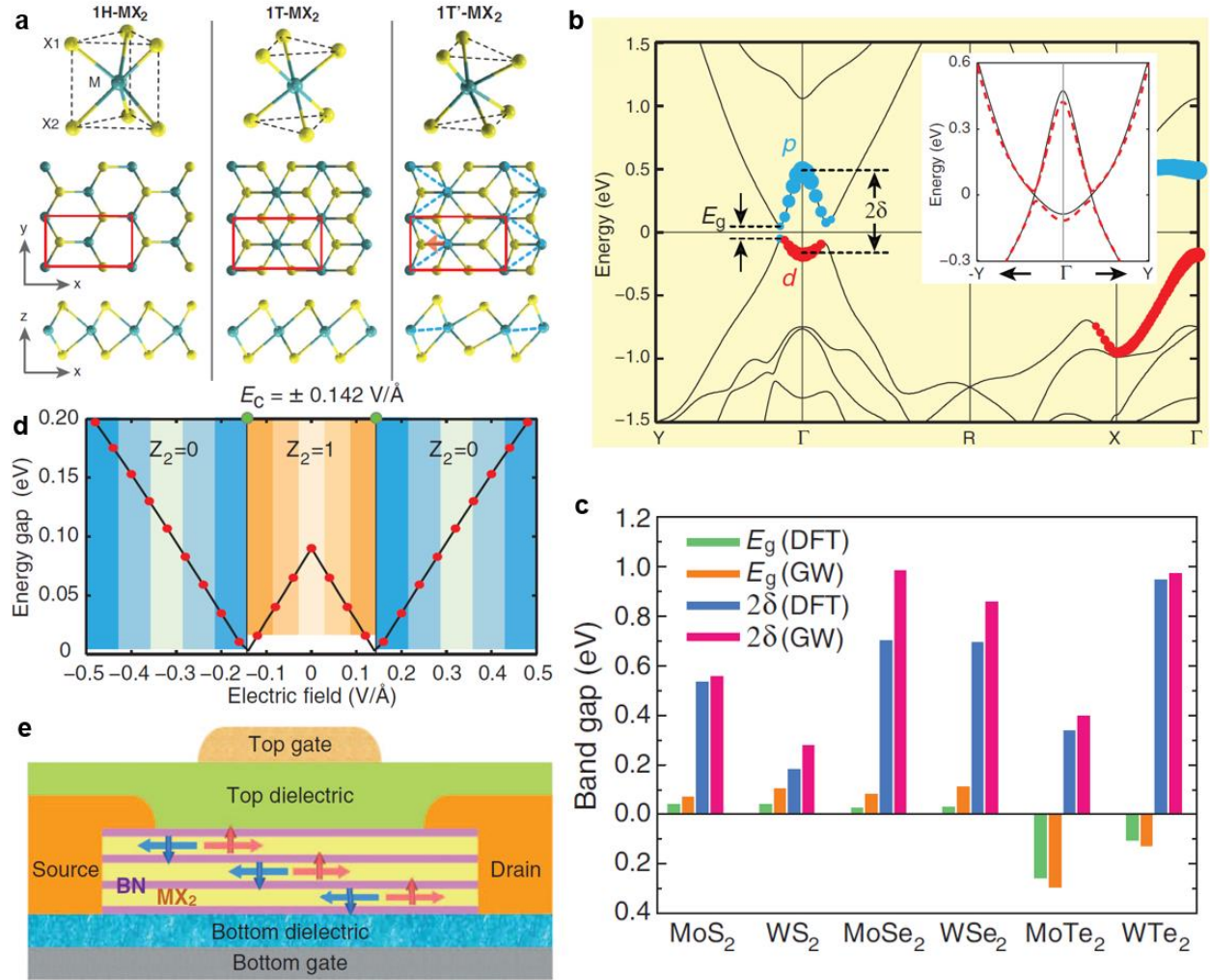


**Figure 12. Prediction of high-temperature quantum spin Hall effect in 2D materials and vdW heterostructures.** (a) Atomic structures of monolayer TMDs in different phases. 1H-MX<sub>2</sub> monolayers are normal semiconductors with direct bandgaps. The 1T phase is typically unstable under free-standing conditions and undergoes spontaneous lattice distortion to convert into the 1T' structure. (b) Calculated electronic band structures of 1T'-MoS<sub>2</sub>, showing the formation of a large inverted gap ( $2\delta$ ) at  $\Gamma$  of approximately 0.6 eV. (c) Calculated fundamental gap ( $E_g$ ) and inverted gap ( $2\delta$ ) of the six 1T'-TMDs. (d) Electrical field controlled topological phase diagram of 1T'-MoS<sub>2</sub>. The electric field breaks the inversion symmetry and introduces strong Rashba splitting of the doubly degenerate bands near the fundamental gap  $E_g$  at the  $\Lambda$  points.  $E_g$  first decreases to zero when the electrical field increases to a critical field strength of 0.142 V/Å and then reopens. This gap-closing transition induces a topological change to a trivial phase, leading to the destruction of helical edge states. (e) The proposed vdW topological field effect transistor consists of multiple monolayers of 1T'-MX<sub>2</sub> separated by thin insulating hBN layers, preventing detrimental topological phase changes while parametrically increasing the number of edge channels. Reprinted and adapted with permission, (a-e) from [233] (AAAS).

High-temperature QSH states were observed in 1T'-MX<sub>2</sub> monolayers and at the phase boundary of 1T'-2H phase lateral junctions, as presented in Fig. 13. By carrying out the processing of the

highly air-sensitive 1T'-phase TMD monolayers in an inert environment, several research groups have reported the QSH effect in 1T'-WTe<sub>2</sub> [240-243]. Wu *et al.* observed all characteristics of the QSH transport through a 2D time-reversal invariant topological insulator in the device made of 1T'-WTe<sub>2</sub> monolayer up to 100 K including: (i) the edge conductance, quantized at  $e^2/h$  per edge, by helical edge modes; (ii) the saturated conductance in the short-edge limit; and (iii) suppression of conductance quantization upon application of a magnetic field owing to the loss of protection by time-reversal symmetry [240], Fig. 13a and 13b.

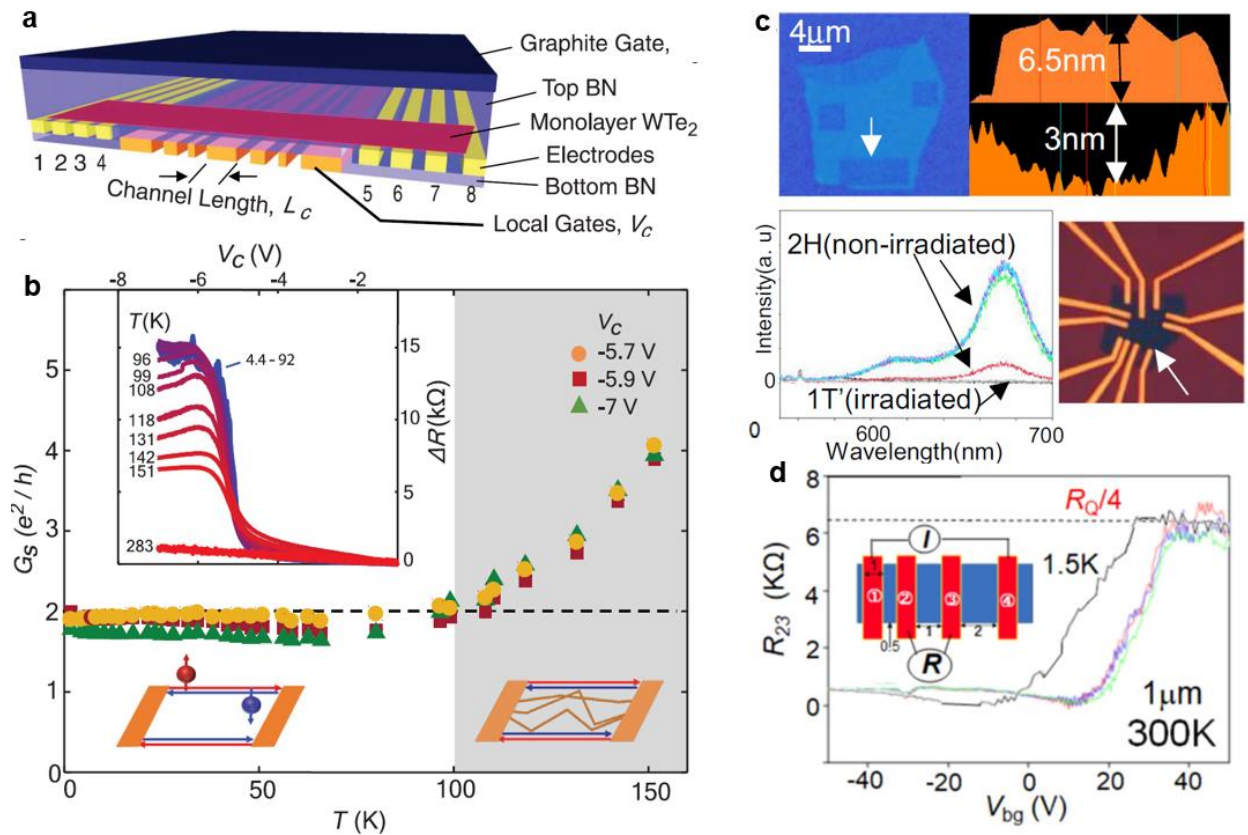


**Figure 13. Observation of the high-temperature quantum spin Hall effect in 2D materials and vdW heterostructures.** (a, b) Device structure and electrical characteristics of 1T'-WTe<sub>2</sub> monolayer device. Below 100 K, the device conductance  $G_s$  remains approximately constant and close to  $2e^2/h$ , indicating that the conductance is dominated by quantum spin Hall effects. Above 100 K, the channel conductance increases rapidly with temperature due to the activation of bulk-conduction channels. (c, d) Evidence of room-temperature quantum spin Hall states at the phase boundary of MoS<sub>2</sub>. The 1T'-phase regions are induced inside the few-layer 2H-MoS<sub>2</sub> using laser irradiation, which is confirmed by Raman spectroscopy (fig. c). The four-probe resistance of the device as a function of back-gate voltage shows plateau-like features with values of  $\sim R_Q/4$ , where the quantum resistance  $R_Q = h/e^2$ , which is similar to properties of the quantum spin Hall phase reported in HgTe quantum well systems. Reprinted and adapted with permission, (a) and (b) from [240] (AAAS), (c) and (d) from [245] (Springer Nature).

Using laser irradiation, Katsuragawa *et al.* induced a 1T'-phase region embedded in an original 2H MoS<sub>2</sub> multilayer [244, 245], which was confirmed by Raman spectroscopy measurement (Fig. 13c). The authors then observed the saturated conductance at  $e^2/2h$  and  $e^2/4h$ , as well as the suppression of conductance quantisation under an externally applied magnetic field in the fabricated devices, as the signatures of the QSH states [245]. The phenomena survive up to 300 K, suggesting the possibility of room-temperature topological devices (Fig. 13d), although further experiments are needed to verify this. Recent advances in the growth of Mo<sub>x</sub>W<sub>1-x</sub>Te<sub>2</sub> alloys, in which their phases can be easily transformed from 2H to 1T (1T') by changing the percentage of transition metals (Mo, W), may provide a test bed for QSH states at the phase boundary [246, 247]. Introducing magnetism into a TI by adding and/or substituting atoms during the growth of 2D materials to form a magnetic TI has also recently attracted attention [248-257]. The discovery of intrinsic magnetic TI in the MnBi<sub>2</sub>Te<sub>4</sub> family [252] and Kagome magnets [254-257] opens new opportunities for exploring rich quantum physics in TI systems.

The concept of electrically controlled topological phases for topological FETs has been realised in several structures such as Bi-based TIs [258, 259], SnTe thin films [260], and few-layer Ge [261]. The search for new TIs with high T<sub>c</sub> and innovative device configurations may enable us to achieve high-performance topological FETs operating even at room temperature [262].

Spin FET, which is usually referred as the Datta-Das spin-FET, is a conceptual spintronic device introduced by Supriyo Datta and Biswajit Das in 1990 [263]. In this device, the current flow is modulated by the electron spin rather than the charge alone. This approach can be achieved because of the Rashba spin-orbit interaction effect, a quantum phenomenon that allows electron spin to be manipulated by an electric field [264]. By tuning the gate voltage, the electron spins can be rotated by any angle between 0° and 180° as they travel through the channel. The spin current can be turned ON or OFF when the spin orientation of the electrons is aligned or misaligned with that of the drain electrode. Although spin-FETs are expected to be faster and more energy-efficient than traditional transistors, the search for semiconductors with strong spin-orbit coupling and sufficiently long spin coherence lengths to prevent the loss of spin information during transport is a great challenge [265-270]. VdW heterostructures provide new opportunities to realise high-performance spin-FETs by combining 2D materials with different functionalities simultaneously. For example, electrically controlled spin currents have been reported at room temperature in various TI/graphene and TMD/graphene heterostructures [271-275]. In these devices, the

combination of the superior spin transport properties of graphene with the strong spin-orbit coupling TI or TMDs allows switching of the spin current in the graphene channel between ON and OFF states by tuning the spin absorption into TI or TMD with a gate voltage, as shown in Fig. 14a and 14b [271]. An alternative spin-tunnel FET can also be built using 2D magnetic materials, as shown in Fig. 14 c and 14d [276]. In this spin-TFET, the electrical field switches the magnetisation configuration of the 2D magnet, leading to the high- and low- tunnelling resistance states of the device [276-280].

The strong dependence of charge-to-spin conversion and spin texture generation on twist angles in graphene-based heterostructures has been theoretically predicted and experimentally observed recently [281, 282]. For example, Yang *et al.* found that changing the twist angle between graphene and WSe<sub>2</sub> layers from 7° to 36.7° reverses the helicity of the spin texture owing to the opposite unconventional Rashba-Edelstein effect [282]. This highlights again the critical role of the twist angle in the interaction of charges and spins at the vdW heterointerfaces.

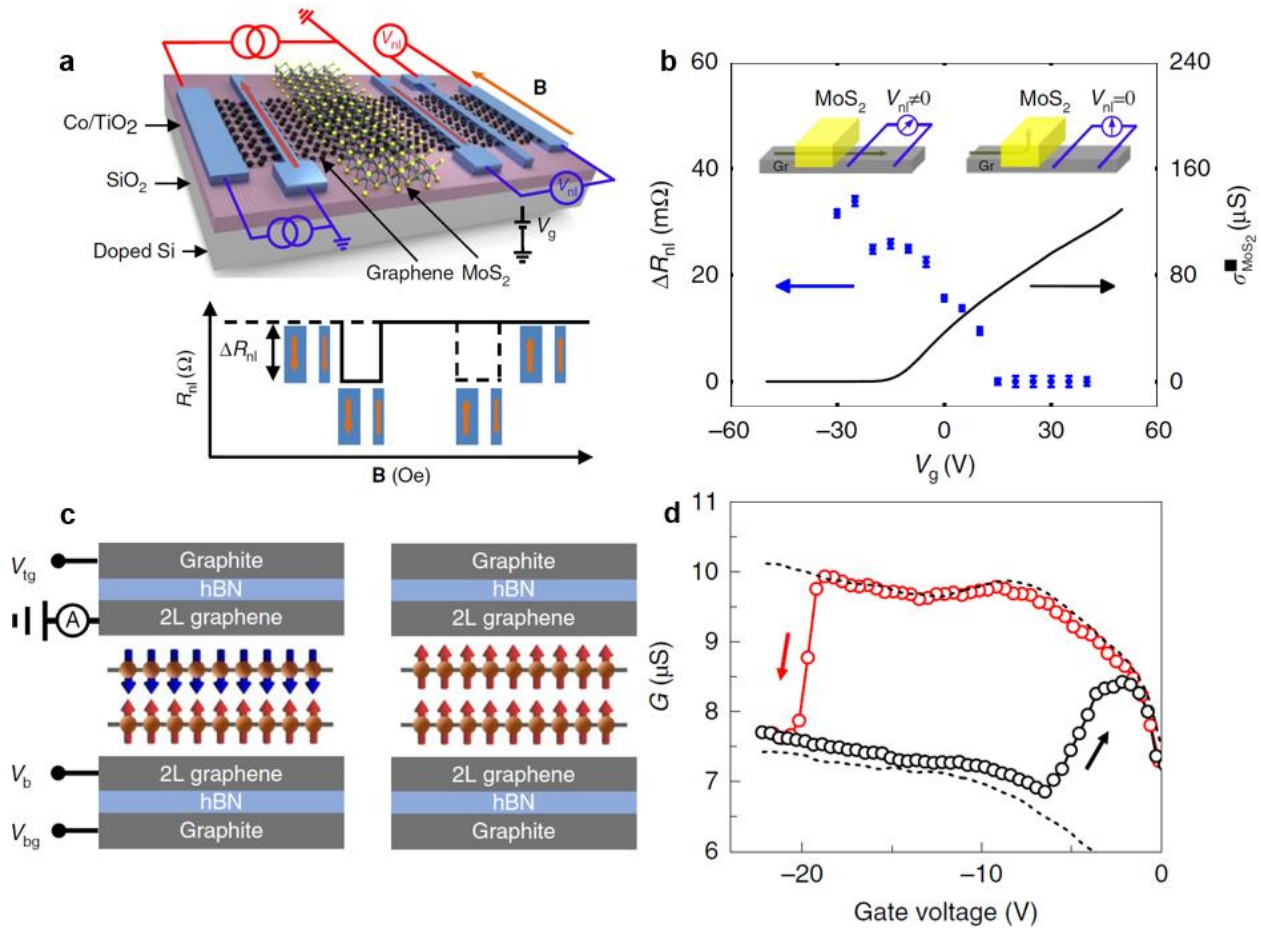


**Figure 14. vdW spin transistors.** (a) Schematic of a spin transistor using graphene/MoS<sub>2</sub> vdW heterostructures. The detection of pure spin currents is carried out with a non-local measurement, where a DC current is injected into graphene from a ferromagnetic Co electrode across a TiO<sub>2</sub> barrier, and a non-local voltage ( $V_{nl}$ ) is measured by a second Co electrode while sweeping the magnetic field. The spin signal is proportional to the amount of spin current that reaches the detector, which is characterized by  $\Delta R_{nl}$ . (b) Gate-modulated spin signal in graphene/MoS<sub>2</sub> heterostructure device (blue circles). The solid black line represents the sheet conductivity of the MoS<sub>2</sub>. The insets show the spin current path (green arrow) in the OFF state (left inset) and ON conducting state (right inset) of MoS<sub>2</sub>. (c) Device schematic of a spin-tunnel FET fabricated using bilayer CrI<sub>3</sub> sandwiched between two graphene contacting layers. The operational principle of this spin-tunnel FET is based on a gate-controlled spin-flip transition and spin filtering in the tunnel junction. In the initial states (left panel), bilayer CrI<sub>3</sub> is an antiferromagnet consisting of two monolayers with antiparallel magnetic moments, resulting in high tunnelling resistance of the junction. Applying an electrical field through the top and back gates switches the bilayer CrI<sub>3</sub> to a ferromagnet through a spin-flip transition, leading to a low resistance of the junction (right panel). (d) Gate-controlled tunnel conductance of a TFET with a bilayer CrI<sub>3</sub> tunnel barrier under a constant magnetic bias of 0.76 T. Black and red symbols correspond to measurements while sweeping the gate voltage forward and backward, respectively. Reprinted and adapted with permission, (a) and (b) from [271] (Springer Nature), (c) and (d) from [276] (Springer Nature).

## 6. Topological superconductivity and Majorana modes

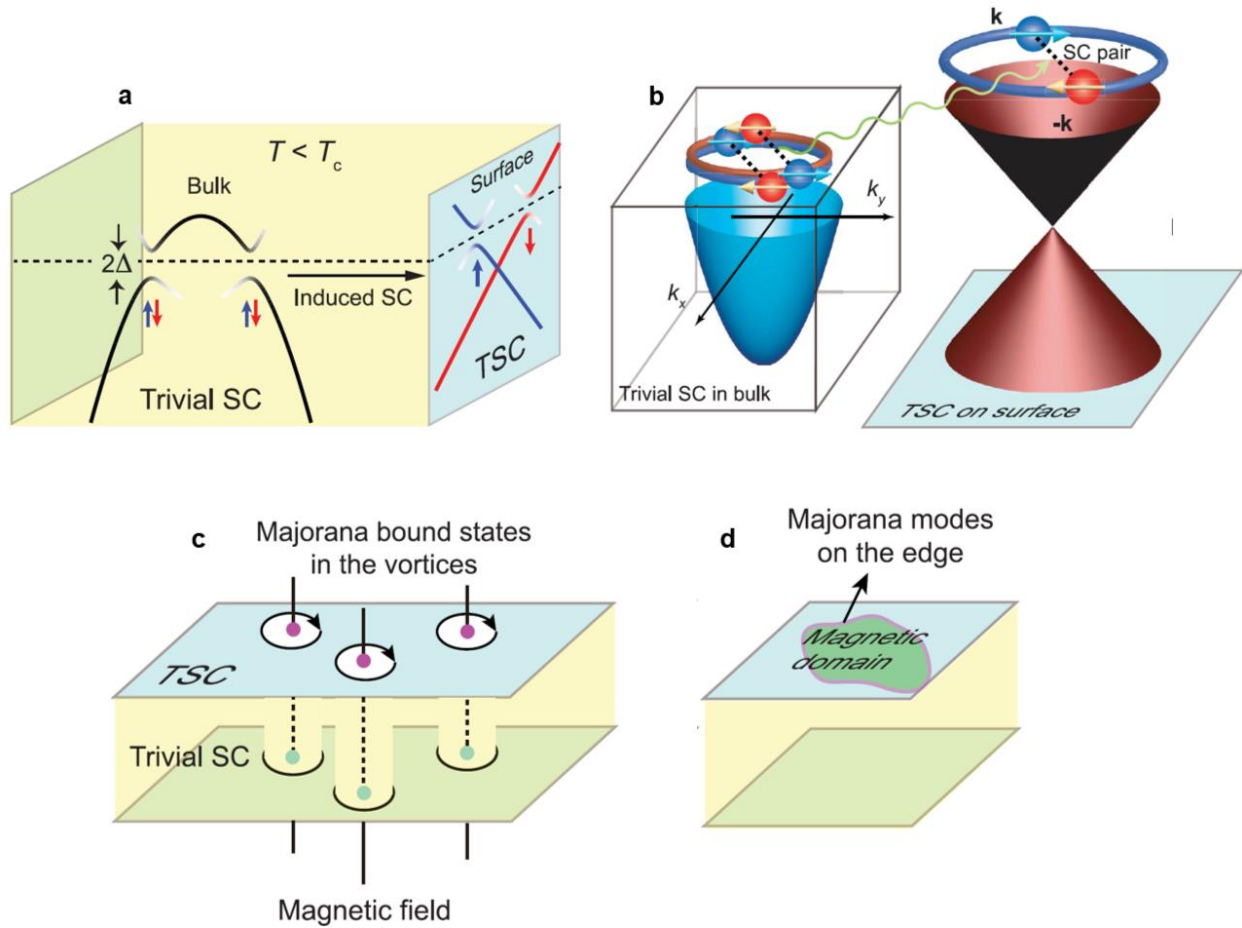


**Figure 15. Topological superconductivity and Majorana modes on the surface.** (a) Schematic visualisation of topological superconductivity in an iron-based superconductor ( $\text{FeTe}_{1-x}\text{Se}_x$ ). The superconducting gaps in the bulk states are topologically trivial due to their spin degeneracy. However, the superconducting gaps of the surface states, which are induced by bulk-to-surface proximity, are topologically superconducting (TSC) because of spin polarisation. Blue and red arrows denote the spin directions. The side surface is shown for convenient visualisation. (b) Band structures with topological superconductivity on surface of  $\text{FeTe}_{0.55}\text{Se}_{0.45}$ . The electrons in the bulk are not spin-polarised, and s-wave superconducting pairing is topologically trivial. The electrons on the surface are induced to form superconducting pairs by the bulk superconductivity. The superconductivity of spin-helical surface states is topologically nontrivial. (c, d) Majorana mode formation on surface of topological superconductor. An applied magnetic field creates vortices, which behave as boundaries for topological superconductivity on the surface, and Majorana bound states are predicted to appear in the vortices. In the case of a magnetic domain existing on the surface that destroys the superconductivity within that domain, itinerant Majorana modes appear along the boundary of the domain. Reprinted and adapted with permission, (a-d) from [289] (AAAS).

In a topological superconducting structure, Cooper pairs can tunnel from the superconductor to the topological insulator surface owing to the superconducting proximity effect, thereby inducing a

superconducting energy gap in the surface states [37]. These surface states are different from those of a single ordinary superconductor because they are not spin-degenerate and contain only half the degrees of freedom of a normal metal [37, 283]. Under certain conditions, the vortices in the superconductor may trap so-called zero-mode, spin-1/2 excitons of very low (zero) energy on the surface, forming a so-called Majorana zero-mode (MZMs) [283]. MZMs have been realised at low temperatures in epitaxially grown nanowires on 3D superconducting substrates and have been engineered for topological qubits [283-288]. Figure 15 represents the visualisation of the band structures of a topological superconductor candidate and the formation of Majorana bound states on its surface [289].

The combination of a 2D topological insulator with a 2D superconductor to form vdW heterostructures appears to be a straightforward route towards topological superconductivity. The evidence of topological superconductivity has been reported in different vdW heterostructures [290-293] such as  $\text{Bi}_2\text{Te}_3/\text{NbSe}_2$ ,  $\text{WTe}_2/\text{NbSe}_2$ ,  $\text{CrBr}_3/\text{NbSe}_2$ , and  $\text{MnBi}_2\text{Te}_4/\text{NbSe}_2$ . Some of these observations are represented in Fig. 16. By manually stacking 1T'- $\text{WTe}_2$  on the surface of superconducting  $\text{NbSe}_2$ , Lüpke *et al.* observed a proximity-induced superconducting gap in the edge region of the  $\text{WTe}_2$  monolayer, as in Fig. 16a and 16b [291]. However, this gap is typically small (below 1 meV), and no zero-bias conductance peak was observed, which could be due to degradation of the surfaces and interfaces of the 2D layers during the sample processing [291]. Kezilebieke *et al.* grew a monolayer ferromagnet,  $\text{CrBr}_3$ , directly on  $\text{NbSe}_2$  using molecular-beam epitaxy in an ultra-high vacuum to obtain a vdW heterostructure with clean edges and interfaces, Fig. 16a [292]. In this heterostructure, topological superconductivity is attributed to a combination of out-of-plane ferromagnetism, superconductivity, and Rashba-type spin-orbit coupling between the ferromagnet and superconductor layers [292]. The scanning tunnelling microscopy spectra of the heterostructure show that a strong zero-bias conductance peak appears at the edge region of the monolayer  $\text{CrBr}_3$  (Fig. 16d and 16e). The observed conductance peak is consistent with the expected Majorana modes along the edge of the magnetic island in the established 2D topological superconductivity [292, 294]. These results confirm the critical role of the interface quality of the vdW heterostructure in achieving strong interfacial coupling.

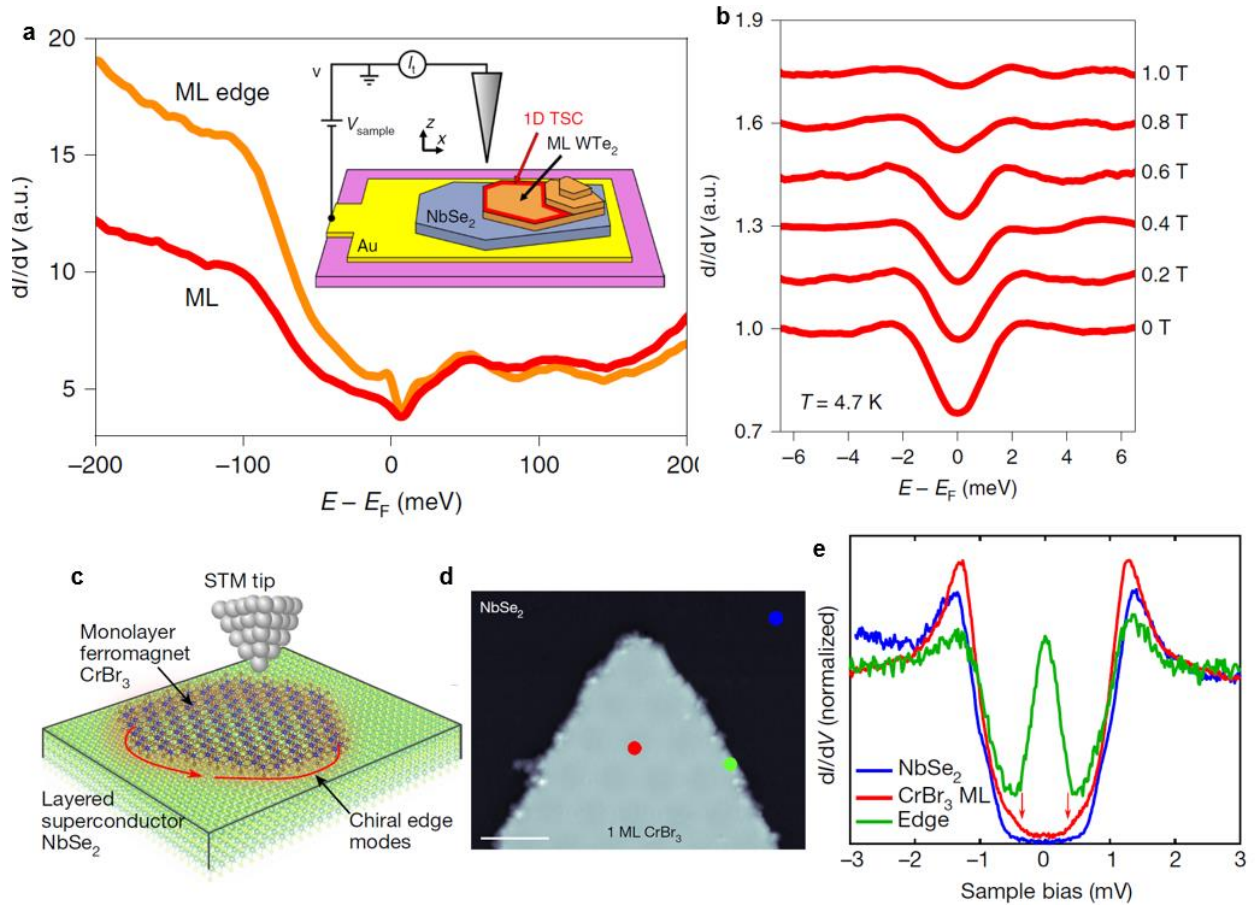


**Figure 16. Observation of topological superconductivity in vdW heterostructures.** (a, b) Differential conductance spectra of monolayer  $\text{WTe}_2$  stacked on  $\text{NbSe}_2$  showing the simultaneous presence of the quantum spin Hall edge state and superconducting gap on  $\text{WTe}_2$ . (c-e) Experimental setup, STM images, and differential conductance spectra for the realisation of topological superconductivity in the  $\text{CrBr}_3/\text{NbSe}_2$  heterostructure. A zero-bias conductance peak appearing inside the superconductor gap is observed along the edge region of the  $\text{CrBr}_3$  island. This zero-bias conductance peak is consistent with the Majorana modes calculated for 2D topological superconductors. Reprinted and adapted with permission, (a, b) from [291] (Springer Nature), (c-e) from [292] (Springer Nature).

Moiré superlattices have recently emerged as attractive systems for exploring QSH states and topological superconductors [295-299]. By fabricating twisted  $\text{MoTe}_2$  homobilayers at small twist angles of 2-4 degrees, several research groups have recently reported the observation of the fractional quantum Hall effect in the absence of a magnetic field [300-304]. The observation of the fractional anomalous Hall effect in these twisted bilayers at filling factors  $\nu = -2/3$  is an important and interesting achievement as it may open the opportunity to realise anyons at zero magnetic field, a key factor for stable quantum qubits [288, 300].

Motivated by the novel quantum phenomena observed in twisted vdW heterostructures, numerous device structures have been theoretically proposed to realise robust Majorana zero modes (MZMs) in these systems [148, 305-307]. We highlight some of them as in Fig. 17. Mercado *et al.* predicted that a structure consisting of a twisted bilayer of a high- $T_c$  superconductor, such as  $\text{Bi}_2\text{Sr}_2\text{CaCu}_2\text{O}_{8+\delta}$  (BSCCO), on the surface of a 3D topological insulator hosts an unpaired MZM in the core of an Abrikosov vortex (Fig. 17 a) [306]. High  $T_c$  of BSCCO induces potentially larger excitation gaps and higher critical temperatures of topological insulator states. In addition, the extremely short coherence length  $\xi$  of this superconductor enhances MZM protection from decoherence effects [306]. Gate engineering to induce a nanowire structure on twisted bilayer graphene stacked on the surface of a TMD monolayer may also give rise to MZMs in the device (Fig. 17b) [307]. This mechanism is similar to the proximity effects observed in epitaxially grown nanowires on conventional superconductors [284]. However, MZM may be formed even at zero magnetic field, depending on the precise symmetry-breaking order [307]. The observation of the quantum spin Hall liquid characteristic in  $\text{RuCl}_3$  makes it a promising material for building vdW heterostructures for the realisation of MZM [308-310]. Halász proposed a device structure for generating and detecting anyons as presented in Fig. 17c [311]. The structure consists of a single layer of Kitaev spin liquid, like  $\text{RuCl}_3$ , on the surface of a monolayer semiconductor, such as  $\text{MoS}_2$  or  $\text{WSe}_2$ , and is engineered in a ring-disk-shaped device. Generation and detection of anyons are carried out through applications of gate voltages,  $V_{\text{disk}}$  and  $V_{\text{ring}}$ , and by measuring the electrical conductance between the two leads [311].

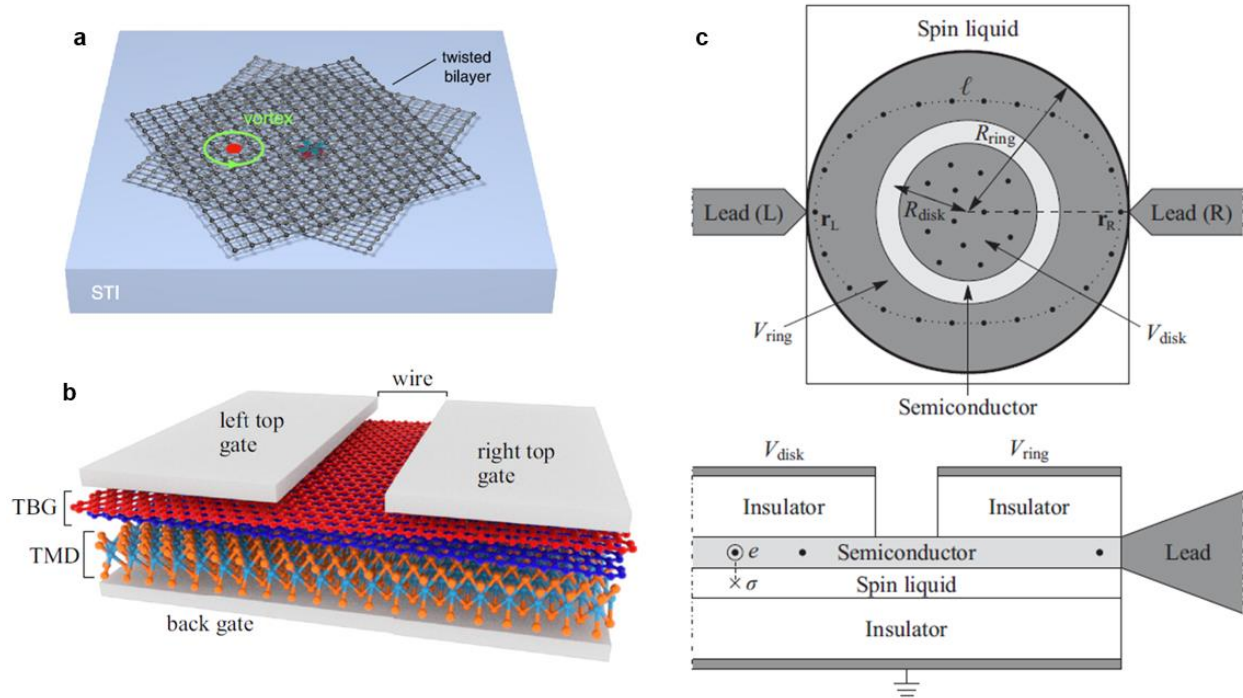


**Figure 17. Proposed vdW heterostructures for realisation of Majorana modes.** (a) Twisted bilayer high- $T_c$  superconductors stacked on the surface of a strong topological insulator generating an unpaired MZM in the core of an Abrikosov vortex. (b) Twisted bilayer graphene on TMD. The left and right top gates induce a nanowire structure on twisted graphene, and the MZM appears at the ends of this wire. The mechanism of MZM formation is similar to the proximity effects observed in epitaxially grown nanowires on conventional superconductors; however, MZM may be formed even at zero magnetic field, depending on the precise symmetry-breaking order. (c) Monolayer TMD on a spin liquid material ( $\text{RuCl}_3$ ) with a ring-disk-shaped device. Kondo coupling stabilises an Ising anyon in  $\text{RuCl}_3$  around each electron in the semiconductor. A single anyon can be generated in the disk-shaped region by gate tuning its electron number to one, while it can be interferometrically detected by measuring the electrical conductance of a ring-shaped region around it, whose electron number is allowed to fluctuate between zero and one. Reprinted and adapted with permission, (a) from [306] (APS), (b) from [307] (APS), (c) from [311] (APS).

## 7. Conclusion and perspective

In summary, we reviewed recent research progress in emergent quantum phenomena in vdW heterostructures, including quantum tunnelling of single and paired particles, exciton condensation, quantum spin Hall states, and topological superconductivity. Interface engineering is a crucial factor for achieving high-temperature-operating quantum devices. Strong interlayer coupling and

tunnelling in the natural homojunction within vdW materials due to clean interfaces and perfect alignment allow the observation of quantum phenomena at high temperatures. Meanwhile, twisted bi- and multilayer structures possess numerous unexpected quantum effects which are still being intensely explored but could contribute to high-temperature quantum phenomena and devices.

As we discuss throughout the paper, the twist angle plays a crucial role in emerging quantum phenomena in vdW heterostructures but is challenging to handle in practice. First, controlling it precisely during device processing is very difficult because the ultralow friction between 2D layers easily induces instabilities and local moiré-noise [312]. Second, changing the twist angle even a fraction of a degree may lead to significant modification of moiré periodicity (in particular for low angles) and thereby the interlayer interaction, which again alters the correlations of charges and spins [102, 313]. Twist-angle programming [312] and quantum twisting microscopy [314] (see Fig. 18) have been recently reported to be useful for exploring high-temperature quantum phenomena in vdW heterostructures at arbitrary twist angles. These techniques allow rotation of the top layer at an accurate specific angle to the bottom layer with continuous ranges, while emerging phenomena from the heterostructure can be investigated *in-situ* by optical/electrical/magnetic measurements. To achieve high-temperature quantum devices with vdW heterostructure, one can start with selecting proper 2D components and then maintaining clean interfaces during device processing to search for optimized twist angle using the quantum twisting microscopy.

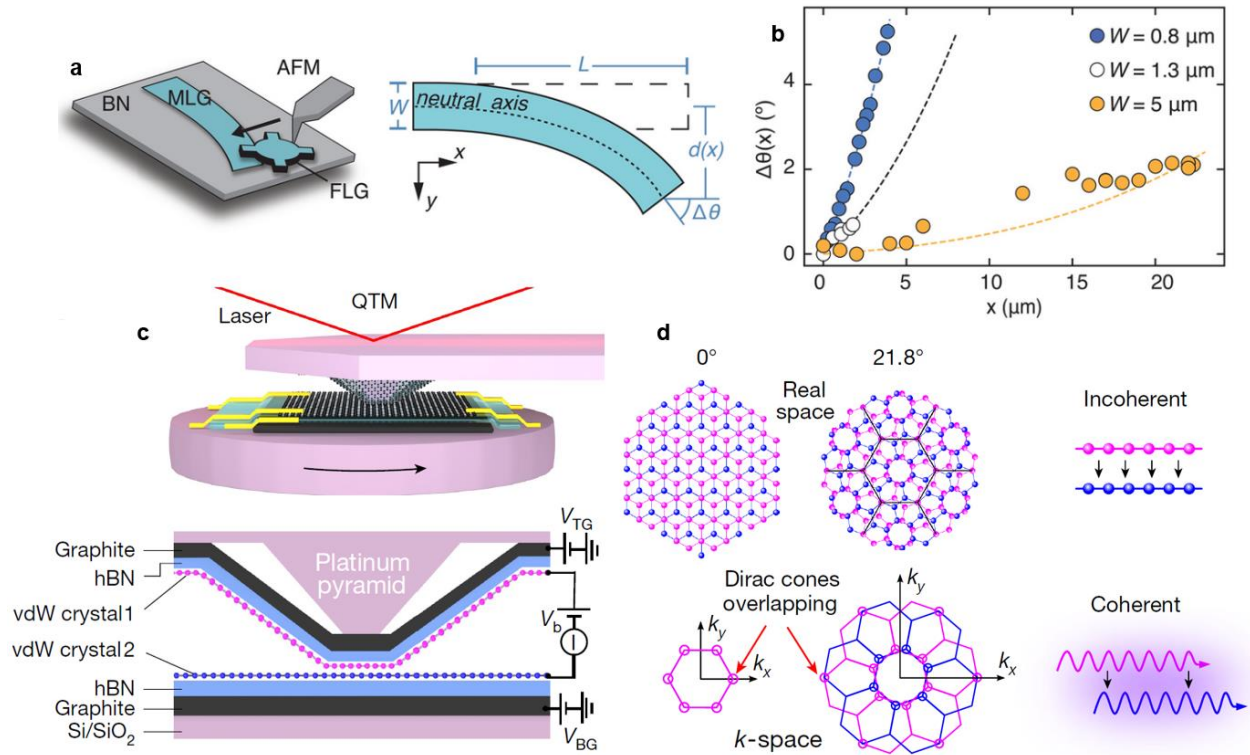


**Figure 18. Programming twist angle and quantum twisting microscopy.** (a) Schematic of bending a 2D material ribbon using a nanomanipulator and the tip of an atomic force microscope. BN: hBN substrate, MLG: monolayer graphene, FLG: few-layer graphite. The FLG manipulator is fabricated with gear-like geometry. The AFM tip slides the manipulator at the end of the MLG ribbon, inducing the bending of the ribbon. Moiré patterns with different periodicities are formed along the MLG ribbon. (b) Twist angle calculated from the measured moiré wavelength as a function of position along the ribbon with three different widths  $W$  shown in (a). (c) Schematic of the quantum twisting microscopy (QTM) and experimental setup for *in-situ* electrical measurements. 2D crystals are deposited on the bottom substrate as well as on the top pyramid-shaped AFM tip located near the edge of the AFM cantilever with electrical contacts. The rotation of the AFM tip allows for continuous control of the relative angle between the tip and the sample, while the electrical properties of the heterostructure can be measured *in-situ*. (d) Real-space and momentum-space registry for commensurate angles of  $0^\circ$  and  $21.8^\circ$  between the top and bottom graphene monolayers. At a twist angle of  $0^\circ$  the Dirac cones of the two layers overlap at the corners of the first Brillouin zone, and at  $\theta = 21.8^\circ$  they overlap at the corners of the third Brillouin zone. Coherent tunnelling across a 2D junction can be achieved by changing the twist angle to form commensurate stackings in real space, for example, at  $\theta = 21.8^\circ$  and  $38.2^\circ$  for a bilayer graphene structure. Reprinted and adapted with permission, (a) and (b) from [312] (AAAS), (c) and (d) from [314] (Springer Nature).

The achievement of record low-average SS values and high on-current in TFETs at room temperature [108] and the observation of exciton condensation and quantum spin Hall above 100 K in 2D materials and vdW heterostructures [184, 240] are very encouraging and promising towards high temperature quantum devices. There are still, however, significant challenges in bringing these exotic materials and quantum functionalities into commercial applications.

High-performance devices and quantum phenomena are usually achieved only in small sample areas, where high-quality 2D materials are produced by mechanical exfoliation. For industrial applications, scalable materials with high quality and robust device processing are necessary. Research and development of wafer-scale growth [315-318], transfer techniques [319-321], pattern engineering [322-324], and 3D integration of 2D materials [325, 326] may eventually enable 2D TFETs to compete with conventional Si-based FETs.

Due to their thinness and the need to form atomically precise junctions without ultrahigh-vacuum conditions as in the case of epitaxial growth, 2D materials and their interfaces are invariably and significantly affected by experimental conditions, resulting in difficulties in terms of reproducibility, consistency, and scalability [327-328]. Today, relatively few research teams are able to fabricate high-quality twisted bilayer structures suitable for observation of quantum phenomena, such as those described in this review [329]. Therefore, the development of clear and robust protocols for vdW heterostructure processing would help accelerate research achievements, as well as more transparent, thorough, and systematic documentation of experimental methodologies and difficulties.

Contact resistance is another severe issue which limits device performance and prevents the observation of quantum phenomena, especially in TMD devices [330-335]. Despite significant efforts have been spent on this issue, achieving low contact resistance for 2D devices is still challenging, mainly because of the strong Fermi level pinning and interface disorder [331, 332]. Recent reports on the use of semimetals or charge-transfer doping for achieving low contact resistance in monolayer TMDs are promising [336-338].

Although signatures of correlated electron-hole pair tunnelling and quantum spin Hall states have been observed at room temperature [192, 245], more theoretical and experimental structures need to be attempted to obtain room-temperature superfluidity and topological superconductors. The recent discoveries of room-temperature topological insulators [339], correlated states in twisted bilayer MoS<sub>2</sub> [158], and quantum valley Hall effect in bilayer graphene [340] may provide the possibility of searching for high-temperature superconductivity and MZMs.

## **Acknowledgements**

The authors thank Cheng Xiang for kindly helping with figure processing. M.-H. D. acknowledges support from the EU Graphene Flagship Core 3 (No. 881603), Villum Experiment (No. 41016), and NNF Biomag (NNF21OC0066526). P. B. acknowledges the support from DFF Metatune (1032-00496B), DFF Tr2DEO (1026-00153A), and NNF Biomag (NNF21OC0066526).

## References

- [1] Strubell E, Ganesh A and McCallum A 2020 Energy and policy considerations for modern deep learning research *Proc. AAAI Conf. Art. Int.* **34** 13693-13696
- [2] Rong H, Zhang H, Xiao S, Li C and Hu C 2016 Optimizing energy consumption for data centers *Renew. Sust. Energ. Rev.* **58** 674-691
- [3] Silva C A, Vilaça R, Pereira A and Bessa R J 2024 A review on the decarbonization of high-performance computing centers *Renew. Sust. Energ. Rev.* **189** 114019
- [4] Lambert S, Heddeghem W V, Vereecken W, Lannoo B, Colle D and Pickavet M 2012 Worldwide electricity consumption of communication networks *Opt. Exp.* **20** B513-B524
- [5] Schaller R R 1997 Moore's law: past, present and future *IEEE Spectrum* **34** 52-59
- [6] Thompson S E, Parthasarathy S. 2006 Moore's law: the future of Si microelectronics *Mater. Today* **9** 20-25
- [7] Bhattacharya D and Jha N K 2014 FinFETs: from devices to architectures *Adv. Electron.* **2014** 65689
- [8] Das R R, Rajalekshmi T R and James A 2024 FinFET to GAA MBCFET: a review and insights *IEEE Acc.* **12** 50556-50577
- [9] Bishop M D, Wong H S P, Mitra S and Shulaker M M 2019 Monolithic 3-D integration *IEEE Micro* **39** 16-27
- [10] Hu C 1993 Future CMOS scaling and reliability *Proc. IEEE* **81** 682-689
- [11] Packan P A 1999 Pushing the limits *Science* **285** 2079-2081
- [12] Waldrop M M 2016 The chips are down for Moore's law *Nature* **530** 144-147
- [13] Cao W et al. 2023 The future transistors *Nature* **620** 501-515
- [14] Pop E, Sinha S and Goodson K E 2006 Heat generation and transport in nanometer-scale transistors *Proc. IEEE* **94**, 1587-1601
- [15] Zhao Y and Qu Y 2019 Impact of self-heating effect on transistor characterization and reliability issues in sub-10 nm technology nodes *IEEE J. Elec. Dev. Soc.* **7** 829-836
- [16] Yan Z, Liu G, Khan J M and Balandin A A 2012 Graphene quilts for thermal management of high-power GaN transistors *Nat. Commun.* **3** 827
- [17] Ferry D K, Weinbub J, Nedjalkov M and Selberherr S 2022 A review of quantum transport in field-effect transistors *Semicond. Sci. Technol.* **37** 043001
- [18] Adrian M I and Heike R 2011 Tunnel field-effect transistors as energy-efficient electronic switches *Nature* **479** 329-337
- [19] Nadeem et al 2021 Overcoming Boltzmann's tyranny in a transistor via the topological quantum field effect *Nano Lett.* **21** 3155-3161
- [20] Lu H and Seabaugh A 2014 Tunnel field-effect transistors: state-of-the-art *IEEE J. Elec. Dev. Soc.* **2** 44-49
- [21] Xue Q K 2011 A topological twist for transistors *Nat. Nanotech.* **6** 197-198
- [22] Giazotto F et al 2003 Ultralow dissipation Josephson transistor *Appl. Phys. Lett.* **83** 2877-2879
- [23] Paolucci F et al 2018 Ultra-efficient superconducting dayem bridge field-effect transistor *Nano Lett.* **18** 4195-4199
- [24] Avci U E, Morris D H and Young I A 2015 Tunnel field-effect transistors: prospects and challenges *IEEE J. Elec. Dev. Soc.* **3** 88-95
- [25] Banerjee S et al 2022 Robust subthermionic topological transistor action via antiferromagnetic exchange *Phys. Rev. Appl.* **18** 054088

- [26] Wray L 2012 Topological transistor *Nat. Phys.* **8** 705-706
- [27] Weber B et al 2024 2024 roadmap on 2D topological insulators *J. Phys. Mater.* **7** 022501
- [28] Ladd T D, Jelezko F, Laflamme R, Nakamura Y, Monroe C and O'Brien J L 2010 Quantum computers *Nature* **464** 45-53
- [29] Steane A 1998 Quantum computing *Rep. Prog. Phys.* **61** 117-173
- [30] Stern A and Lindner N H 2013 Topological quantum computation-from basic concepts to first experiments *Science* **339** 1179-1184
- [31] Breunig O and Ando Y 2021 Opportunities in topological insulator devices *Nat. Rev. Phys.* **4** 184-193
- [32] Gyongyosi L and Imre S 2019 A Survey on quantum computing technology *Comput. Sci. Rev.* **31** 51-71
- [33] de Leon N P et al 2021 Materials challenges and opportunities for quantum computing hardware *Science* **372** 253
- [34] Burkard G, Ladd T D, Pan A, Nichol J M and Petta J R 2023 Semiconductor spin qubits *Rev. Mod. Phys.* **95** 025003
- [35] Hasan M Z and Kane C L 2010 Colloquium: Topological insulators *Rev. Mod. Phys.* **82** 3045
- [36] Flensberg K, von Oppen F and Stern A 2021 Engineered platforms for topological superconductivity and Majorana zero modes *Nat. Rev. Mater.* **6** 944-958
- [37] Frolov S M, Manfra M J and Sau J D 2020 Topological superconductivity in hybrid devices *Nat. Phys.* **16** 718-724
- [38] Theis T N and Wong H-S P 2017 The end of Moore's law: a new beginning for information technology *Comput. Sci. Eng.* **19** 41-50
- [39] Zhu E, Zhang Z and Wang C 2023 Editorial: Emerging chip materials and devices for post Moore's era *Front. Mater.* **10** 1224537
- [40] Björk M T, Knoch J, Schmid H, Riel H, and Riess W 2008 Silicon nanowire tunneling field-effect transistors *Appl. Phys. Lett.* **92** 193504
- [41] Desjardins M M et al 2019 Synthetic spin-orbit interaction for Majorana devices *Nat. Mater.* **18** 1060-1064
- [42] Aghaee et al 2023 InAs-Al hybrid devices passing the topological gap protocol *Phys. Rev. B* **107** 245423
- [43] Keimer B and Moore J 2017 The physics of quantum materials *Nat. Phys.* **13** 1045-1055
- [44] von Klitzing K et al 2020 40 years of the quantum Hall effect *Nat. Rev. Phys.* **2** 397-401
- [45] Novoselov K S, Mishchenko A, Carvalho A, and Castro Neto A H 2016 2D materials and van der Waals heterostructures *Science* **353** aac 9439
- [46] Liu Y et al 2016 Van der Waals heterostructures and device *Nat. Rev. Mater.* **1** 16042
- [47] Lemme M C, Akinwande D, Huyghebaert C and Stampfer C 2022 2D materials for future heterogeneous electronics *Nat. Commun.* **13** 1392
- [48] Wei T et al 2022 Two dimensional semiconducting materials for ultimately scaled transistors *iScience* **25** 105160
- [49] Li C et al 2020 Two-dimensional materials for next-generation computing technologies *Nat. Nano.* **15** 545-557
- [50] Kim K S et al 2023 The future of two-dimensional semiconductors beyond Moore's law *Nat. Nano.* **19** 895-906
- [51] Kang J-H et al 2023 Monolithic 3D integration of 2D materials-based electronics towards ultimate edge computing solutions *Nat. Mater.* **22** 1470-1477

- [52] Novoselov K S *et al* 2007 Room-temperature quantum Hall effect in graphene *Science* **315** 1379
- [53] Lee C H *et al* 2014 Atomically thin p-n junctions with van der Waals heterointerfaces *Nat. Nano.* **9** 676-681
- [54] Pal A *et al* 2023 Quantum-engineered devices based on 2D materials for next-generation information processing and storage *Adv. Mater* **35** 2109894
- [55] Gupta S, Wu W, Huang S and Yakobson B I 2023 Single-photon emission from two-dimensional materials to a brighter future *J. Phys. Chem. Lett.* **14** 3274-3284
- [56] Sierra J F, Fabian J, Kawakami R K, Roche S, and Valenzuela S O 2021 Van der Waals heterostructures for spintronics and opto-spintronics *Nat. Nano.* **16** 856-868
- [57] Yurgens A A 2000 Intrinsic Josephson junctions: recent developments *Supercond. Sci. Technol.* **13** R85
- [58] Kleiner R, Koelle D, Ludwig F and Clarke J 2004 Superconducting quantum interference devices: State of the art and applications *Proc. IEEE* **92** 1534-1548
- [59] Makhlin Y, Schön G and Shnirman A 2001 Quantum-state engineering with Josephson-junction devices *Rev. Mod. Phys.* **73** 357
- [60] Fagaly R L 2006 Superconducting quantum interference device instruments and applications *Rev. Sci. Instrum.* **77** 101101
- [61] Wendin G and Shumeiko V S 2007 Quantum bits with Josephson junctions *Low Temp. Phys.* **33** 724-744
- [62] Blatt J M, Boer K W, and Brandt W 1962 Bose-Einstein condensation of excitons *Phys. Rev.* **126** 1691
- [63] Butov L V, Lai C W, Ivanov A L, Gossard A C, and Chemla D S 2002 Towards Bose-Einstein condensation of excitons in potential traps *Nature* **417** 47
- [64] Lozovik Y E and Yudson V I 1976 A new mechanism for superconductivity: pairing between spatially separated electrons and holes *Sov. Phys. JETP.* **44** 389
- [65] Nandi D *et al* 2012 Exciton condensation and perfect Coulomb drag *Nature* **488**, 481-184
- [66] Su U J and MacDonald A H 2008 How to make a bilayer exciton condensate flow *Nat. Phys.* **4** 799-802
- [67] Esaki L 1958 New phenomenon in narrow Germanium p-n junctions *Phys. Rev.* **109** 603
- [68] Schmid H, Bessire C, Björk M T, Schenk A, and Riel H 2012 Silicon nanowire Esaki diodes *Nano Lett.* **12** 699-703
- [69] Fung W Y, Chen L, Lu W 2011 Esaki tunnel diodes based on vertical Si-Ge nanowire heterojunctions *Appl. Phys. Lett.* **99** 092108
- [70] Sarkar D *et al* 2015 A subthermionic tunnel field-effect transistor with an atomically thin channel *Nature* **526** 91-95
- [71] Nourbakhsh A, Zubair A, Dresselhaus M S, Palacios T 2016 Transport properties of a MoS<sub>2</sub>/WSe<sub>2</sub> heterojunction transistor and its potential for application *Nano Lett.* **16** 1359-1366
- [72] Roy T *et al* 2016 2D-2D tunneling field-effect transistors using WSe<sub>2</sub>/SnSe<sub>2</sub> heterostructures *Appl. Phys. Lett.* **108** 083111
- [73] Doan M-H *et al* Charge transport in MoS<sub>2</sub>/WSe<sub>2</sub> van der Waals heterostructure with tunable inversion layer *ACS Nano* **11** 3832-3840
- [74] Liu X *et al* 2017 Modulation of quantum tunneling via a vertical two-dimensional black phosphorus and molybdenum disulfide p-n junction *ACS Nano* **11** 9143-9150

- [75] Lin Y-C *et al* 2015 Atomically thin resonant tunnel diodes built from synthetic van der Waals heterostructures *Nat. Commun.* **6** 7311
- [76] Yan R *et al* 2015 Esaki diodes in van der Waals heterojunctions with broken-gap energy band alignment *Nano Lett.* **15** 5791-5798
- [77] Kim J H *et al* 2024 Room temperature negative differential resistance with high peak current in MoS<sub>2</sub>/WSe<sub>2</sub> heterostructures *Nano Lett.* **24** 2561-2566
- [78] Xiong X *et al* 2020 A transverse tunnelling field-effect transistor made from a van der Waals heterostructure *Nat. Electron.* **3** 106-112
- [79] Sajjad R. N, Chern W, Hoyt J. L and Antoniadis D A 2016 Trap assisted tunneling and its effect on subthreshold swing of tunnel FETs *IEEE Tran. Elec. Dev.* **63** 4380-4387
- [80] Bessire C D, Björk M T, Schmid H, Schenk A, Reuter K B and Riel H 2011 Trap-assisted tunneling in Si-InAs nanowire heterojunction tunnel diodes *Nano Lett.* **11** 4195-4199
- [81] Beyerlein I J, Demkowicz M J, Misra A and Uberuaga B P 2015 Defect-interface interactions *Prog. Mater. Sci.* **74** 125-210
- [82] Haigh S J *et al* 2012 Cross-sectional imaging of individual layers and buried interfaces of graphene-based heterostructures and superlattices *Nat. Mater.* **11** 764-767
- [83] Chou H, Ismach A, Ghosh R, Ruoff R S and Dolocan A 2015 Revealing the planar chemistry of two-dimensional heterostructures at the atomic level *Nat. Commun.* **6** 7482
- [84] Khestanova E, Guinea F, Fumagalli L, Geim A K and Grigorieva I V 2016 Universal shape and pressure inside bubbles appearing in van der Waals heterostructures *Nat. Commun.* **7** 12587
- [85] Pizzocchero F *et al* 2016 The hot pick-up technique for batch assembly of van der Waals heterostructures *Nat. Commun.* **7** 11894
- [86] Purdie D G *et al* 2018 Cleaning interfaces in layered materials heterostructures *Nat. Commun.* **9** 5387
- [87] Liu S *et al* 2023 Two-step flux synthesis of ultrapure transition-metal dichalcogenides *ACS Nano* **17** 16587-16596
- [88] Huang C *et al* 2014 Lateral heterojunctions within monolayer MoSe<sub>2</sub>-WSe<sub>2</sub> semiconductors *Nat. Mater.* **13** 1096-1101
- [89] Cai Z, Liu B, Zou X and Cheng H-M 2018 Chemical vapor deposition growth and applications of two-dimensional materials and their heterostructure *Chem. Rev.* **118** 6091-6133
- [90] Liu C *et al* 2024 Understanding epitaxial growth of two-dimensional materials and their homostructures *Nat. Nano.* **19** 907-918
- [91] Fan S *et al* 2019 Tunable negative differential resistance in van der Waals heterostructures at room temperature by tailoring the interface *ACS Nano* **13** 8193-8201
- [92] Chae S H *et al* 2016 Oxidation effect in octahedral hafnium disulfide thin film *ACS Nano* **10** 1309-1316
- [93] Britnell L *et al* 2013 Resonant tunnelling and negative differential conductance in graphene transistors *Nat. Commun.* **4** 1794
- [94] Zhang Z *et al* 2023 Toward high-peak-to-valley-ratio graphene resonant tunneling diodes, *Nano Lett.* **23** 8132
- [95] Jiang *et al* 2020 Schottky-barrier quantum well in two-dimensional semiconductor nanotransistors *Mater. Today Phys.* **15** 100275
- [96] Sharma *et al* 2024 Transport spectroscopy study of minibands in MoS<sub>2</sub> moiré superlattices *Phys. Rev. B* **109** 195106

- [97] Kudrynskyi Z R *et al* 2020 Resonant tunnelling into the two-dimensional subbands of InSe layers *Commun. Phys.* **3** 16
- [98] Kinoshita K *et al* 2022 Resonant tunneling between quantized subbands in van der Waals double quantum well structure based on few-layer WSe<sub>2</sub> *Nano Lett.* **22** 4640-4645
- [99] Kastner M A 1992 The single-electron transistor *Rev. Mod. Phys.* **64** 849
- [100] Ihn T *et al* 2010 Graphene single-electron transistors *Mater. Today* **13** 44-50
- [101] Song J C W and Gabor N M 2018 Electron quantum metamaterials in van der Waals heterostructures *Nat. Nano.* **13** 986-993
- [102] Kuzmina A *et al* 2021 Resonant light emission from graphene/hexagonal boron nitride/graphene tunnel junctions *Nano Lett.* **21** 8332-8339
- [103] Srivastava P K *et al* 2021 Resonant tunnelling diodes based on twisted black phosphorus homostructures *Nat. Electron.* **4** 269-276
- [104] Hasan M. Z *et al* 2021 Weyl, Dirac and high-fold chiral fermions in topological quantum matter *Nat. Rev. Mater.* **6** 784-803
- [105] Xia H *et al* 2022 Pristine PN junction toward atomic layer devices *Light Sci. Appl.* **11** 170
- [106] Fukui T *et al* 2024 Single-gate MoS<sub>2</sub> tunnel FET with a thickness-modulated homojunction *ACS Appl. Mater. Inter.* **16** 8993-9001
- [107] Li L *et al* 2014 Black phosphorus field-effect transistors *Nat. Nano.* **9** 372-377
- [108] Kim S *et al* 2020 Thickness-controlled black phosphorus tunnel field-effect transistor for low-power switches *Nat. Nano.* **15** 203-206
- [109] Doganov R A *et al* 2014 Transport properties of pristine few-layer black phosphorus by van der Waals passivation in an inert atmosphere *Nat. Commun.* **6** 6647
- [110] Yue *et al* 2016 Passivated ambipolar black phosphorus transistors *Nanoscale* **8** 12773-12779
- [111] Abate Y *et al* 2018 Recent progress on stability and passivation of black phosphorus *Adv. Mater.* **30** 1704749
- [112] Si M *et al* 2018 Steep-slope hysteresis-free negative capacitance MoS<sub>2</sub> transistors *Nat. Nano.* **13** 24-28
- [113] McGuire F A *et al* 2017 Sustained Sub-60 mV/decade Switching via the Negative Capacitance Effect in MoS<sub>2</sub> Transistors *Nano Lett.* **17** 4801-4806
- [114] Wang Y *et al* 2020 Record-low subthreshold-swing negative-capacitance 2D field-effect transistors *Adv. Mater.* **32** 2005353
- [115] Shukla N *et al* 2015 A steep-slope transistor based on abrupt electronic phase transition *Nat. Commun.* **6** 7812
- [116] Das S and Das S 2022 An ultra-steep slope two-dimensional strain effect transistor *Nano Lett.* **22** 9252-9259
- [117] Qiu C *et al* 2018 Dirac-source field-effect transistors as energy-efficient, high-performance electronic switches *Science* **361** 387-392
- [118] Tang Z *et al* 2021 A steep-slope MoS<sub>2</sub>/Graphene Dirac-source field-effect transistor with a large drive current *Nano Lett.* **21** 1758-1764
- [119] Wang S *et al* 2023 Cold source field-effect transistors: Breaking the 60-mV/decade switching limit at room temperature *Phys. Rep.* **1013** 1-33
- [120] Gundapaneni S *et al* 2012 Effect of band-to-band tunneling on junctionless transistors *IEEE Tran. Elec. Dev.* **59** 1023-1029
- [121] Lee T *et al* 2024 Junctionless negative-differential-resistance device using 2D van-der-Waals layered materials for ternary parallel computing *Adv. Mater.* **36** 2310015

- [122] Bardeen J, Cooper L N and Schrieffer J R 1957 Theory of Superconductivity *Phys. Rev.* **108** 1175
- [123] Webb G W, Marsiglio F and Hirsch J E 2015 Superconductivity in the elements, alloys and simple compounds *Physica C* **514** 17-27
- [124] Josephson B D 1974 The discovery of tunnelling supercurrents *Rev. Mod. Phys.* **46** 251
- [125] Yabuki N *et al* 2016 Supercurrent in van der Waals Josephson junction *Nat. Commun.* **7** 10616
- [126] Xia F, Wang H, Xiao D, Dubey M and Ramasubramaniam A 2014 Two-dimensional material nanophotonics *Nat. Photon.* **8** 899-907
- [127] Gong C and Zhang X 2019 Two-dimensional magnetic crystals and emergent heterostructure devices *Science* **363** 706
- [128] Qiu D *et al* 2021 Recent advances in 2D superconductors *Adv. Mater.* **33** 2006124
- [129] Lee J *et al* 2019 Planar graphene Josephson coupling via van der Waals superconducting contacts *Curr. Appl. Phys.* **19** 251-255
- [130] Li J *et al* 2021 Printable two-dimensional superconducting monolayers *Nat. Mater.* **20** 181-187
- [131] Ai L *et al* 2021 Van der Waals ferromagnetic Josephson junctions *Nat. Commun.* **12** 6580
- [132] Idzuchi H *et al* 2021 Unconventional supercurrent phase in Ising superconductor Josephson junction with atomically thin magnetic insulator *Nat. Commun.* **12** 5332
- [133] Qiu G *et al* 2023 Emergent ferromagnetism with superconductivity in Fe(Te,Se) van der Waals Josephson junctions *Nat. Commun.* **14** 6691
- [134] Choi Y-B *et al* 2020 Evidence of higher-order topology in multilayer WTe<sub>2</sub> from Josephson coupling through anisotropic hinge states *Nat. Mater.* **19** 974-979
- [135] Gilbert W *et al* 2023 On-demand electrical control of spin qubits *Nat. Nano.* **18** 131-136
- [136] Niknam M *et al* 2022 Quantum control of spin qubits using nanomagnets *Commun. Phys.* **5** 284
- [137] Wu H *et al* 2022 The field-free Josephson diode in a van der Waals heterostructure *Nature* **604** 653-656
- [138] Wang C *et al* 2024 Two-dimensional van der Waals superconductor heterostructures: Josephson junctions and beyond *Precis. Chem.* **2** 273–281
- [139] Yu Y *et al* 2019 High-temperature superconductivity in monolayer Bi<sub>2</sub>Sr<sub>2</sub>CaCu<sub>2</sub>O<sub>8+δ</sub>. *Nature* **575** 156-163
- [140] Koelle D, Kleiner R, Ludwig F, Dantsker E, and John Clarke J 1999 High-transition-temperature superconducting quantum interference devices *Rev. Mod. Phys.* **71** 631
- [141] Chiarello F 2000 Quantum computing with superconducting quantum interference devices: a possible strategy *Phys. Lett. A* **277** 189-193
- [142] De Simoni G *et al* 2018 Metallic supercurrent field-effect transistor *Nat. Nano.* **13** 802-805
- [143] Golokolenov I *et al* 2021 On the origin of the controversial electrostatic field effect in superconductors *Nat. Commun.* **12** 2747
- [144] Senapati K *et al* 2011 Spin-filter Josephson junctions *Nat. Mater.* **10** 849-852
- [145] Nakagawa Y 2021 Gate-controlled BCS-BEC crossover in a two-dimensional superconductor *Science* **372** 190-195
- [146] Ghosh S *et al* 2024 High-temperature Josephson diode *Nat. Mater.* **23** 612-618
- [147] Liao M *et al* 2018 Superconductor–insulator transitions in exfoliated Bi<sub>2</sub>Sr<sub>2</sub>CaCu<sub>2</sub>O<sub>8+δ</sub> flakes *Nano Lett.* **18** 5660-5665

- [148] BroSCO V *et al* 2024 Superconducting qubit based on twisted cuprate van der Waals heterostructures *Phys. Rev. Lett.* **132** 017003
- [149] Schrade C *et al* 2022 Protected hybrid superconducting qubit in an array of gate-tunable Josephson interferometers *PRX Quantum* **3** 030303
- [150] Cao Y *et al* 2018 Unconventional superconductivity in magic-angle graphene superlattices *Nature* **556** 43-50
- [151] Cao Y *et al* 2018 Correlated insulator behaviour at half-filling in magic-angle graphene superlattices *Nature* **556** 80-84
- [152] Sharpe A L *et al* 2019 Emergent ferromagnetism near three-quarters filling in twisted bilayer graphene *Science* **365** 605-608
- [153] Prance J R and Shalom M B 2021 Building devices in magic-angle graphene *Nat. Nano.* **16** 745-747
- [154] Díez-Mérida *et al* 2023 Symmetry-broken Josephson junctions and superconducting diodes in magic-angle twisted bilayer graphene *Nat. Commun.* **14** 2396
- [155] de Vries F K *et al* 2021 Gate-defined Josephson junctions in magic-angle twisted bilayer graphene *Nat. Nano.* **16** 760-763
- [156] Rodan-Legrain D *et al* 2021 Highly tunable junctions and non-local Josephson effect in magic-angle graphene tunnelling devices *Nat. Nano* **16** 769-775
- [157] Park J M *et al* 2022 Robust superconductivity in magic-angle multilayer graphene family *Nat. Mater.* **21** 877-883
- [158] Wu F *et al* 2023 Giant correlated gap and possible room-temperature correlated states in twisted bilayer MoS<sub>2</sub> *Phys. Rev. Lett.* **131** 256201
- [159] Keimer B *et al* 2015 From quantum matter to high-temperature superconductivity in copper oxides *Nature* **518** 179-186
- [160] S Hüfner *et al* 2008 Two gaps make a high-temperature superconductor? *Rep. Prog. Phys.* **71** 062501
- [161] Orenstein J and Millis A J 2000 Advances in the Physics of High-Temperature Superconductivity *Science* **288** 468-474
- [162] Eisenstein J P and MacDonald A H 2004 Bose–Einstein condensation of excitons in bilayer electron systems *Nature* **432** 691-694
- [163] Combescot M *et al* 2017 Bose–Einstein condensation and indirect excitons: a review *Rep. Prog. Phys.* **80** 066501
- [164] Eisenstein J P 2014 Exciton condensation in bilayer quantum Hall systems *Annu. Rev. Condens. Matter Phys.* **5** 159.
- [165] Muraki K 2017 Exciting double bilayers *Nat. Phys.* **13** 726-728
- [166] Butov L V *et al* 1994 Condensation of indirect excitons in coupled AlAs/GaAs quantum wells *Phys. Rev. Lett.* **73** 304
- [167] Kasprzak J *et al* 2006 Bose-Einstein condensation of exciton polaritons *Nature* **443** 409-414
- [168] Anankine R *et al* 2017 Quantized vortices and four-component superfluidity of semiconductor excitons *Phys. Rev. Lett.* **118** 127402
- [169] Wang R, Sedrakyan T A, Wang B, Du L and Du R-R 2023 Excitonic topological order in imbalanced electron-hole bilayers *Nature* **619** 57-62
- [170] Butov L V 2003 Exciton condensation in coupled quantum wells *Sol. Stat. Commun.* **127** 89-98

- [171] Min H, Bistritzer R, Su J-J and MacDonald A H 2008 Room-temperature superfluidity in graphene bilayers *Phys. Rev. B* **78** 121401(R)
- [172] Li J I A, Taniguchi T, Watanabe K, Hone J, and Dean C R 2017 Excitonic superfluid phase in double bilayer graphene *Nat. Phys.* **13** 751-755
- [173] Liu X, Watanabe K, Taniguchi T, Halperin B I and Kim P 2017 Quantum Hall drag of exciton condensate in graphene *Nature Phys* **13** 746-750
- [174] Regan E C *et al* 2022 Emerging exciton physics in transition metal dichalcogenide heterobilayers *Nat. Rev. Mater.* **7** 778-795
- [175] Hong X *et al* 2014 Ultrafast charge transfer in atomically thin MoS<sub>2</sub>/WS<sub>2</sub> heterostructures *Nat. Nano.* **9** 682-686
- [176] P. Rivera *et al* 2015 Observation of long-lived interlayer excitons in monolayer MoSe<sub>2</sub>-WSe<sub>2</sub> heterostructures *Nat. Commun.* **6** 6242
- [177] Fang H *et al* 2014 Strong interlayer coupling in van der Waals heterostructures built from single-layer chalcogenides *Proc. Natl. Acad. Sci. U.S.A.* **111** 6198-6202
- [178] Jauregui L A *et al* 2019 Electrical control of interlayer exciton dynamics in atomically thin heterostructures *Science* **366** 870-875
- [179] Unuchek U *et al* 2018 Room-temperature electrical control of exciton flux in a van der Waals heterostructure *Nature* **560** 340-344
- [180] Wang L *et al* 2023 Exciton-assisted electron tunnelling in van der Waals heterostructure *Nat. Mater.* **22** 1094-1099
- [181] Fogler M M, Butov L V and Novoselov K S 2014 High-temperature superfluidity with indirect excitons in van der Waals heterostructures *Nat. Commun.* **5** 4555
- [182] Gupta S, Kutana A and Yakobson B I 2020 Heterobilayers of 2D materials as a platform for excitonic superfluidity *Nat. Commun.* **11** 2989
- [183] Debnath B *et al* 2017 Exciton condensate in bilayer transition metal dichalcogenides: Strong coupling regime *Phys. Rev. B* **96** 174504
- [184] Wang Z *et al* 2019 Evidence of high-temperature exciton condensation in two-dimensional atomic double layers *Nature* **574** 76-80
- [185] J. Choi *et al* 2021 Twist angle-dependent interlayer exciton lifetimes in van der Waals heterostructures *Phys. Rev. Lett.* **126** 047401
- [186] Kunstmann J *et al* 2018 Momentum-space indirect interlayer excitons in transition-metal dichalcogenide van der Waals heterostructures *Nat. Phys.* **14** 801-805
- [187] Nayak P K *et al* 2017 Probing evolution of twist-angle-dependent interlayer excitons in MoSe<sub>2</sub>/WSe<sub>2</sub> van der Waals heterostructures *ACS Nano* **11** 4041-4050
- [188] Chen S *et al* 2024 Twist angle-dependent interlayer hybridized exciton lifetimes in van der Waals heterostructures *Nanoscale* **16** 14089-14095
- [189] Shi A *et al* 2024 The interlayer twist effectively regulates interlayer excitons in InSe/Sb van der Waals heterostructure *npj Comp. Mater.* **10** 190
- [190] Saigal N *et al* 2024 Collective charge excitations between Moiré minibands in twisted WSe<sub>2</sub> bilayers probed with resonant inelastic light scattering *Phys. Rev. Lett.* **133** 046902
- [191] Shi Q *et al* 2022 Bilayer WSe<sub>2</sub> as a natural platform for interlayer exciton condensates in the strong coupling limit *Nat. Nano.* **17** 577-582
- [192] Doan M-H, Roy S, Zhou Y and Bøggild P 2023 Signature of correlated electron-hole pair tunneling in multilayer WSe<sub>2</sub> at room temperature *Appl. Phys. Lett.* **123** 143504
- [193] Siao M D *et al* 2018 Two-dimensional electronic transport and surface electron accumulation in MoS<sub>2</sub> *Nat. Commun.* **9** 1442

- [194] Li H-M, Lee D, Qu D, Liu X, Ryu J, Seabaugh A and Yoo W J 2015 Ultimate thin vertical p–n junction composed of two-dimensional layered molybdenum disulfide *Nat. Commun.* **6** 6564
- [195] Yamamoto M, Nakaharai S, Ueno K and Tsukagoshi K 2016 Self-limiting oxides on WSe<sub>2</sub> as controlled surface acceptors and low-resistance hole contacts *Nano Lett.* **16** 2720-2727
- [196] Liu Y *et al* 2017 Vertical charge transport and negative transconductance in multilayer molybdenum disulfides *Nano Lett.* **17** 5495-5501
- [197] Das S and Appenzeller J 2013 Where does the current flow in two-dimensional layered systems? *Nano Lett.* **13** 3396-3402
- [198] Tran S *et al* 2017 Surface transport and quantum Hall effect in ambipolar black phosphorus double quantum wells *Sci. Adv.* **3** e1603179
- [199] Doan M-H *et al* 2019 Room-temperature mesoscopic fluctuations and coulomb drag in multilayer WSe<sub>2</sub> *Adv. Mater.* **31** 1900154
- [200] Rickhaus P *et al* 2021 Correlated electron-hole state in twisted double-bilayer graphene *Science* **373** 1257-1260
- [201] Khanin Y N, Vdovin E E, Dubrovskii Y V and Henini M 2006 Experimental observation of phase coherence in bilayer systems in the absence of a magnetic field *JETP Lett.* **84** 209-213
- [202] Xie M and MacDonald A H 2018 Electrical reservoirs for bilayer excitons *Phys. Rev. Lett.* **121** 067702
- [203] Burg G W *et al* 2018 Strongly enhanced tunneling at total charge neutrality in double-bilayer graphene-WSe<sub>2</sub> heterostructures *Phys. Rev. Lett.* **120** 177702
- [204] Lin K A *et al* 2022 Emergence of interlayer coherence in twist-controlled graphene double layers *Phys. Rev. Lett.* **129** 187701
- [205] Jeon J *et al* 2015 Layer-controlled CVD growth of large-area two-dimensional MoS<sub>2</sub> films *Nanoscale* **7** 1688-1695
- [206] Yang Z and Hao J 2016 Progress in pulsed laser deposited two-dimensional layered materials for device applications *J. Mater. Chem. C* **4** 8859-8878
- [207] Mandyam S V, Kim H M and Drndić M 2020 Large area few-layer TMD film growths and their applications *J. Phys. Mater.* **3** 024008
- [208] Byrnes T, Kim N and Yamamoto Y 2014 Exciton-polariton condensates *Nat. Phys.* **10** 803-813
- [209] Anton-Solanas C *et al* 2021 Bosonic condensation of exciton–polaritons in an atomically thin crystal *Nat. Mater.* **20** 1233-1239
- [210] Ardizzone V *et al* 2019 Emerging 2D materials for room-temperature polaritonics *Nanophoton.* **8** 1547-1558.
- [211] Yuan W *et al* 2024 Electrical switching of the edge current chirality in quantum anomalous Hall insulators *Nat. Mater.* **23** 58-64
- [212] Seradjeh B, Moore J E and Franz M 2009 Exciton condensation and charge fractionalization in a topological insulator film *Phys. Rev. Lett.* **103** 066402
- [213] Kim Y, Hankiewicz E M and Gilbert M J 2012 Topological excitonic superfluids in three dimensions *Phys. Rev. B* **86** 184504
- [214] Hou Y *et al* 2019 Millimetre-long transport of photogenerated carriers in topological insulators *Nat. Commun.* **10** 5723
- [215] Syperek M *et al* 2022 Observation of room temperature excitons in an atomically thin topological insulator *Nat. Commun.* **13** 6313

- [216] Ulman K and Su Ying Quek S Y 2021 Organic-2D Material Heterostructures: A promising platform for exciton condensation and multiplication *Nano Lett.* **21** 8888-8894
- [217] Guo H, Zhang X and Lu G 2022 Tuning moiré excitons in Janus heterobilayers for high-temperature Bose-Einstein condensation *Sci. Adv.* **8** eabp9757
- [218] Wu X *et al* 2024 Exciton polariton condensation from bound states in the continuum at room temperature *Nat. Commun.* **15** 3345
- [219] Kędziora M *et al* 2024 Predesigned perovskite crystal waveguides for room-temperature exciton-polariton condensation and edge lasing *Nat. Mater.* **2024** DOI:10.1038/s41563-024-01980-3
- [220] Liu Y *et al* 2021 Moiré superlattices and related moiré excitons in twisted van der Waals heterostructures *Chem. Soc. Rev.* **50** 6401-6422
- [221] Huang D, Choi J, Shih C-K and Li X Excitons in semiconductor moiré superlattices *Nat. Nano.* **17** 227-238
- [222] Xiong R *et al* 2023 Correlated insulator of excitons in WSe<sub>2</sub>/WS<sub>2</sub> moiré superlattices *Science* **380** 860-864
- [223] Zhang Z *et al* 2022 Correlated interlayer exciton insulator in heterostructures of monolayer WSe<sub>2</sub> and moiré WS<sub>2</sub>/WSe<sub>2</sub> *Nat. Phys.* **18** 1214-1220
- [224] Bange J P *et al* 2024 Probing electron-hole Coulomb correlations in the exciton landscape of a twisted semiconductor heterostructure *Sci. Adv.* **10** eadi1323
- [225] Zheng H *et al* Localization-enhanced moiré exciton in twisted transition metal dichalcogenide heterotrilayer superlattices *Light Sci. Appl.* **12** 117
- [226] Qi X-L and Zhang S-C 2011 Topological insulators and superconductors *Rev. Mod. Phys.* **83** 1057
- [227] Kane C L and Mele E J 2005 Quantum spin Hall effect in graphene *Phys. Rev. Lett.* **95** 226801
- [228] Lodge M S, Yang S A, Mukherjee S and Weber B 2021 Atomically thin quantum spin Hall insulators *Adv. Mater.* **33** 2008029
- [229] König M *et al* 2007 Quantum spin Hall insulator state in HgTe quantum wells *Science* **319** 766-770
- [230] Zhang H *et al* 2009 Topological insulators in Bi<sub>2</sub>Se<sub>3</sub>, Bi<sub>2</sub>Te<sub>3</sub> and Sb<sub>2</sub>Te<sub>3</sub> with a single Dirac cone on the surface *Nat. Phys.* **5** 438-442
- [231] Chen Y L *et al* 2009 Experimental realization of a three-dimensional topological insulator Bi<sub>2</sub>Te<sub>3</sub> *Science* **325** 178-181
- [232] Nowack K 2013 Imaging currents in HgTe quantum wells in the quantum spin Hall regime *Nat. Mater.* **12** 787-791
- [233] Qian X, Liu J, Fu L and Li J 2014 Quantum spin Hall effect in two-dimensional transition metal dichalcogenides *Science* **346** 1344-1347
- [234] Cho S *et al* 2015 Phase patterning for ohmic homojunction contact in MoTe<sub>2</sub> *Science* **349** 625-628
- [235] Voiry D, Mohite A and Chhowalla M 2015 Phase engineering of transition metal dichalcogenides *Chem. Soc. Rev.* **44** 2702-2712
- [236] Deng K *et al* 2016 Experimental observation of topological Fermi arcs in type-II Weyl semimetal MoTe<sub>2</sub> *Nat. Phys.* **12** 1105-1110
- [237] Choi Y-G *et al* 2023 Pseudo-hydrodynamic flow of quasiparticles in semimetal WTe<sub>2</sub> at room temperature *Small* **19** 2206604

- [238] Xu Y *et al* 2013 Large-gap quantum spin Hall insulators in Tin films *Phys. Rev. Lett.* **111** 136804
- [239] Ohfuchi M and Sekine A 2023 Quantum spin Hall states in 2D monolayer WTe<sub>2</sub>/MoTe<sub>2</sub> lateral heterojunctions for topological quantum computation *ACS Appl. Nano Mater.* **6** 2020-2026
- [240] Wu S *et al* 2018 Observation of the quantum spin Hall effect up to 100 kelvin in a monolayer crystal *Science* **359** 76-79
- [241] Tang S *et al* 2017 Quantum spin Hall state in monolayer 1T'-WTe<sub>2</sub> *Nat. Phys.* **13** 683-687
- [242] Fei Z *et al* 2017 Edge conduction in monolayer WTe<sub>2</sub> *Nat. Phys.* **13** 677-682
- [243] Fatemi V *et al* 2018 Electrically tunable low-density superconductivity in a monolayer topological insulator *Science* **362** 926-929
- [244] Mine H *et al* 2019 Laser-beam-patterned topological insulating states on thin semiconducting MoS<sub>2</sub> *Phys. Rev. Lett.* **123** 146803
- [245] Katsuragawa N *et al* 2020 Room-temperature quantum spin Hall phase in laser-patterned few-layer 1T- MoS<sub>2</sub> *Commun. Mater.* **1** 51
- [246] Oliver S M *et al* 2017 The structural phases and vibrational properties of Mo<sub>1-x</sub>W<sub>x</sub>Te<sub>2</sub> alloys *2D Mater.* **4** 045008
- [247] Jin W *et al* 2018 Phase transition and electronic structure evolution of MoTe<sub>2</sub> induced by W substitution *Phys. Rev. B* **98** 144114
- [248] Li J *et al* 2019 Intrinsic magnetic topological insulators in van der Waals layered MnBi<sub>2</sub>Te<sub>4</sub>-family materials *Sci. Adv.* **5** eaaw5685
- [249] Yun S J *et al* 2020 Ferromagnetic order at room temperature in monolayer WSe<sub>2</sub> semiconductor via vanadium dopant *Adv. Sci.* **7** 1903076
- [250] Otrokov M M *et al* 2019 Prediction and observation of an antiferromagnetic topological insulator *Nature* **576** 416-422
- [251] Wu J *et al* 2019 Natural van der Waals heterostructural single crystals with both magnetic and topological properties *Sci. Adv.* **5** eaax9989
- [252] Deng Y *et al* 2020 Quantum anomalous Hall effect in intrinsic magnetic topological insulator MnBi<sub>2</sub>Te<sub>4</sub> *Science* **367** 895-900
- [253] Liu C *et al* 2020 Robust axion insulator and Chern insulator phases in a two-dimensional antiferromagnetic topological insulator *Nat. Mater.* **19** 522-527
- [254] Zhao H *et al* 2021 Cascade of correlated electron states in the kagome superconductor CsV<sub>3</sub>Sb<sub>5</sub> *Nature* **599** 216-221
- [255] Bernevig B A, Felser C and Beidenkopf H 2022 Progress and prospects in magnetic topological materials *Nature* **603** 41-51
- [256] Yin J-X, Lian B and Hasan M Z 2022 Topological kagome magnets and superconductors *Nature* **612** 647-657
- [257] Xu X, Yin J-X, Qu Z and Jia S 2023 Quantum interactions in topological R166 kagome magnet *Rep. Prog. Phys.* **86** 114502
- [258] Checkelsky J G 2011 Bulk band gap and surface state conduction observed in voltage-tuned crystals of the topological insulator Bi<sub>2</sub>Se<sub>3</sub> *Phys. Rev. Lett.* **106** 196801
- [259] Xiu F *et al* 2011 Manipulating surface states in topological insulator nanoribbons *Nat. Nanotech.* **6** 216-221
- [260] Liu J *et al* 2014 Spin-filtered edge states with an electrically tunable gap in a two-dimensional topological crystalline insulator *Nat. Mater.* **13** 178-183

- [261] Bampoulis P *et al* 2023 Quantum spin Hall states and topological phase transition in germanene *Phys. Rev. Lett.* **130** 196401
- [262] Jana K and Muralidharan B 2022 Robust all-electrical topological valley filtering using monolayer 2D-Xenes *npj 2D Mater. Appl.* **6** 19
- [263] Datta S and Das B 1990 Electronic analog of the electro-optic modulator *Appl. Phys. Lett.* **56** 665-667
- [264] Manchon A *et al* 2015 New perspectives for Rashba spin-orbit coupling *Nat. Mater.* **14** 871-882
- [265] Hammar P R and Johnson M 2002 Detection of spin-polarized electrons injected into a two-dimensional electron gas *Phys. Rev. Lett.* **88** 066806
- [266] Koo H C *et al* 2009 Control of spin precession in a spin-injected field effect transistor *Science* **325** 1515-1518
- [267] Malik G F A *et al* 2020 Spin field effect transistors and their applications: A survey *Micro. J.* **106** 104924
- [268] Ciorga M 2016 Electrical spin injection and detection in high mobility 2DEG systems *J. Phys: Cond. Matt.* **28** 453003
- [269] Ahn E C 2020 2D materials for spintronic devices *npj 2D Mater. Appl.* **4** 17
- [270] Wei D S *et al* 2018 Electrical generation and detection of spin waves in a quantum Hall ferromagnet *Science* **362** 229-233
- [271] Yan W *et al* 2016 A two-dimensional spin field-effect switch *Nat. Commun.* **7** 13372
- [272] Benítez L A *et al* 2020 Tunable room-temperature spin galvanic and spin Hall effects in van der Waals heterostructures *Nat. Mater.* **19** 170-175
- [273] Zhao B *et al* 2020 Observation of charge to spin conversion in Weyl semimetal WTe<sub>2</sub> at room temperature *Phys. Rev. Res.* **2** 013286
- [274] Khokhriakov D *et al* 2020 Gate-tunable spin-galvanic effect in graphene-topological insulator van der Waals heterostructures at room temperature *Nat. Commun.* **11** 3657
- [275] Powalla L *et al* 2022 Berry curvature-induced local spin polarisation in gated graphene/WTe<sub>2</sub> heterostructures *Nat. Commun.* **13** 3152
- [276] Jiang S *et al* 2019 Spin tunnel field-effect transistors based on two-dimensional van der Waals heterostructures *Nat. Electron.* **2** 159-63
- [277] Song *et al* 2018 Giant tunneling magnetoresistance in spin-filter van der Waals heterostructures *Science* **360** 1214-1218
- [278] Jiang S *et al* 2018 Controlling magnetism in 2D CrI<sub>3</sub> by electrostatic doping *Nat. Nano.* **13** 549-553
- [279] Huang B *et al* 2018 Electrical control of 2D magnetism in bilayer CrI<sub>3</sub> *Nat. Nano.* **13** 544-548
- [280] Liu P *et al* 2023 Recent advances in 2D van der Waals magnets: Detection, modulation, and applications *iScience* **26** 107584
- [281] David A *et al* 2019 Induced spin-orbit coupling in twisted graphene-transition metal dichalcogenide heterobilayers: twistrionics meets spintrionics *Phys. Rev. B* **100** 085412
- [282] Yang H *et al* 2024 Twist-angle-tunable spin texture in WSe<sub>2</sub>/graphene van der Waals heterostructures *Nat. Mater.* (2024) DOI: 10.1038/s41563-024-01985-y
- [283] Sarma S D *et al* 2015 Majorana zero modes and topological quantum computation *npj Quantum Infor.* **1** 15001
- [284] Mourik V *et al* 2012 Signatures of Majorana fermions in hybrid superconductor-semiconductor nanowire devices *Science* **336** 1003-1007

- [285] Wilczek F 2009 Majorana returns *Nat. Phys.* **5** 614-618
- [286] Alicea J 2012 New directions in the pursuit of Majorana fermions in solid state system *Rep. Prog. Phys.* **75** 076501
- [287] Lutchyn R M *et al* 2018 Majorana zero modes in superconductors-semiconductor heterostructures *Nat. Rev. Mater.* **3** 52-68
- [288] Yazdani A *et al* 2023 Hunting for Majoranas *Science* **380** eade0850
- [289] Zhang P *et al* 2018 Observation of topological superconductivity on the surface of an iron-based superconductor *Science* **360** 182-186
- [290] Xu J-P *et al* 2015 Experimental detection of a Majorana mode in the core of a magnetic vortex inside a topological insulator-superconductor  $\text{Bi}_2\text{Te}_3/\text{NbSe}_2$  heterostructure *Phys. Rev. Lett.* **114** 017001
- [291] Lüpke F *et al* 2020 Proximity-induced superconducting gap in the quantum spin Hall edge state of monolayer  $\text{WTe}_2$  *Nat. Phys.* **16** 526-530
- [292] Kezilebieke S *et al* 2020 Topological superconductivity in a van der Waals heterostructure *Nature* **588** 424-428
- [293] Dong P *et al* 2024 Proximity-effect-induced superconductivity in a van der Waals heterostructure consisting of a magnetic topological insulator and a conventional superconductor *Phys. Rev. B* **109** L140503
- [294] Palacio-Morales A *et al* 2019 Atomic-scale interface engineering of Majorana edge modes in a 2D magnet-superconductor hybrid system *Sci. Adv.* **5**: eaav6600
- [295] Mak K M and Shan J 2022 Semiconductor moiré materials *Nat. Nano.* **17** 686-695
- [296] Kennes D M *et al* 2021 Moiré heterostructures as a condensed-matter quantum simulator *Nat. Phys.* **17** 155-163
- [297] Anderson E *et al* 2023 Programming correlated magnetic states with gate-controlled moiré geometry *Science* **381** 325-330
- [298] Wu F *et al* 2019 Topological insulators in twisted transition metal dichalcogenide homobilayers *Phys. Rev. Lett.* **122** 086402
- [299] Devakul T, Crépel V, Zhang Y and Fu L 2021 Magic in twisted transition metal dichalcogenide bilayers *Nat. Commun.* **12** 6730
- [300] Park H *et al* 2023 Observation of fractionally quantized anomalous Hall effect *Nature* **622** 74-79
- [301] Xu F *et al* 2023 Observation of integer and fractional quantum anomalous Hall effects in twisted bilayer  $\text{MoTe}_2$  *Phys. Rev. X* **13** 031037
- [302] Cai J *et al* 2023 Signatures of fractional quantum anomalous Hall states in twisted  $\text{MoTe}_2$  *Nature* **622** 63-68
- [303] Zeng Y *et al* 2023 Thermodynamic evidence of fractional Chern insulator in moiré  $\text{MoTe}_2$ , *Nature* **622** 69-73
- [304] Kang K *et al* 2024 Evidence of the fractional quantum spin Hall effect in moiré  $\text{MoTe}_2$  *Nature* **628** 522-526
- [305] Luo X-J, Qiu W-X and Wu F 2024 Majorana zero modes in twisted transition metal dichalcogenide homobilayers *Phys. Rev. B* **109** L041103
- [306] Mercado A, Sahoo S and Franz M 2022 High-temperature Majorana zero modes *Phys. Rev. Lett.* **128** 137002
- [307] Thomson A, Sorensen I M, Nadj-Perge S and Alicea J 2022 Gate-defined wires in twisted bilayer graphene: From electrical detection of intervalley coherence to internally engineered Majorana modes *Phys. Rev. B* **105** L081405

- [308] Do S H *et al* 2017 Majorana fermions in the Kitaev quantum spin system  $\alpha$ -RuCl<sub>3</sub> *Nat. Phys.* **13** 1079-1084
- [309] Kasahara Y *et al* 2018 Majorana quantization and half-integer thermal quantum Hall effect in a Kitaev spin liquid *Nature* **559** 227-231
- [310] Yokoi T *et al* 2021 Half-integer quantized anomalous thermal Hall effect in the Kitaev material candidate  $\alpha$ -RuCl<sub>3</sub> *Science* **373** 568-572
- [311] Halász G B 2023 Gate-controlled anyon generation and detection in Kitaev spin liquids *Phys. Rev. Lett.* **132** 206501
- [312] Kapfer M *et al* 2023 Programming twist angle and strain profiles in 2D materials *Science* **381** 677-681
- [313] Tsang C S *et al* 2024 Polar and quasicrystal vortex observed in twisted-bilayer molybdenum disulfide *Science* **386** 198-205
- [314] Inbar A *et al* 2023 The quantum twisting microscope *Nature* **614** 682-687
- [315] Xu X *et al* 2022 Growth of 2D materials at the wafer scale *Adv. Mater.* **34** 2108258
- [316] Choi S H *et al* 2022 Large-scale synthesis of graphene and other 2D materials towards industrialization *Nat. Commun.* **13** 1484
- [317] Zhong Lin *et al* 2016 2D materials advances: from large scale synthesis and controlled heterostructures to improved characterization techniques, defects and applications *2D Mater.* **3** 042001
- [318] Zhou Z *et al* 2023 Stack growth of wafer-scale van der Waals superconductor heterostructures *Nature* **621** 499-505
- [319] Schranghamer T F, Sharma M, Singh R and Das S 2021 Review and comparison of layer transfer methods for two-dimensional materials for emerging applications *Chem. Soc. Rev.* **50** 11032-11054
- [320] Dong W, Dai Z, Liu L and Zhang Z 2023 Toward Clean 2D Materials and Devices: Recent Progress in Transfer and Cleaning Methods *Adv. Mater.* **36** 2303014
- [321] Cheliotis I and Zergioti I 2024 A review on transfer methods of two-dimensional materials *2D Mater.* **11** 022004
- [322] Stanford M G, Rack P D and Jariwala D 2018 Emerging nanofabrication and quantum confinement techniques for 2D materials beyond graphene *npj 2D Mater. Appl.* **2** 20
- [323] Liu S *et al* 2022 Nanopatterning technologies of 2D materials for integrated electronic and optoelectronic devices *Adv. Mater.* **34** 2200734
- [324] Danielsen D R *et al* 2021 Super-resolution nanolithography of two-dimensional materials by anisotropic etching *ACS Appl. Mater. Inter.* **13** 41886-41894
- [325] Huang X, Liu C and Zhou P 2022 2D semiconductors for specific electronic applications: from device to system *npj 2D Mater. Appl.* **6** 51
- [326] Jayachandran D, Sakib N U and Das S 2024 3D integration of 2D electronics *Nat. Rev. Electr. Eng.* **1** 300-316
- [327] Bøggild P 2023 Research on scalable graphene faces a reproducibility gap *Nat. Commun.* **14** 1126
- [328] Heiserer S *et al* 2023 Controllable and reproducible growth of transition metal dichalcogenides by design of experiments *Adv. Elec. Mater.* **9** 2300281
- [329] Lau C N, Bockrath M W, Mak K F and Zhang Z 2022 Reproducibility in the fabrication and physics of moiré materials *Nature* **602** 41-50
- [330] Schulman D S, Arnold A J and Das S 2018 Contact engineering for 2D materials and devices *Chem. Soc. Rev.* **47** 3037-3058

- [331] Chen R-S, Ding G, Zhou Y, Han S-T 2021 Fermi-level Depinning of 2D Transition Metal Dichalcogenide Transistors *J. Mater. Chem. C* **9** 11407-11427
- [332] Sun C *et al* 2022 Fermi level depinning in two-dimensional materials using a fluorinated bilayer graphene barrier *ACS Appl. Electron. Mater.* **4** 3955-3961
- [333] Zheng Y, Gao J, Han C, and Chen W 2021 Ohmic Contact Engineering for Two-Dimensional Materials *Cell Rep. Phys. Sci.* **2** 100298
- [334] Batool S, Idrees M, Han S-T, Roy V R L and Zho Y 2023 Electrical contacts with 2D materials: current developments and future prospects *Small* **9** 2206550
- [335] Kim B, Lee S and Park J-H 2024 Innovations of metallic contacts on semiconducting 2D transition metal dichalcogenides toward advanced 3D-structured field-effect transistors *Nanoscale Horiz.* **9** 1417-1431
- [336] Shen P-C *et al* 2021 Ultralow contact resistance between semimetal and monolayer semiconductors *Nature* **593** 211-217
- [337] Li W *et al* 2023 Approaching the quantum limit in two-dimensional semiconductor contacts *Nature* **613** 274-279
- [338] Pack *et al* 2024 Charge-transfer contacts for the measurement of correlated states in high-mobility WSe<sub>2</sub> *Nat. Nano.* **19** 948-954
- [339] N. Shumiya *et al* 2022 Evidence of a room-temperature quantum spin Hall edge state in a higher-order topological insulator *Nat. Mater.* **21** 1111-1115
- [340] Huang K, Fu H, Watanabe K, Taniguchi T and Zhu J 2024 High-temperature quantum valley Hall effect with quantized resistance and a topological switch *Science* **385** 657-661